Received: 17 June 2022 | Revised: 28 November 2022 | Accepted: 9 December 2022

DOI: 10.1002/cav.2138

RESEARCH ARTICLE

WILEY

Evaluation of particle-based smoothed particle hydrodynamics boundary handling approaches in computer animation

Rustam Akhunov[1] | **Rene Winchenbach**[2] | **Andreas Kolb**[1]

[1]Computer Graphics, Siegen University, Siegen, Germany

[2]Physics-based Simulations, Technical University Munich, Munich, Germany

Correspondence
Rustam Akhunov, Computer Graphics, Siegen University, Siegen, Germany.
Email: rustam.akhunov@uni-siegen.de

Funding information
Deutsche Forschungsgemeinschaft, Grant/Award Number: Ko-2960-15/1

Abstract

Boundary handling is an important aspect of fluid simulation, and several boundary handling approaches exist in smoothed particle hydrodynamics (SPH), which have individual strengths and weaknesses. However, comparing different boundary handling approaches is challenging as there is no common basis for evaluations, that is, no universal set of experiments with quantitative evaluation across different methods, especially within computer animation where many evaluations rely mainly on visual perception. This article proposes a set of experiments to aid the evaluation of the main categories of fluid-boundary interactions that are important in computer animation, that is, *no motion* (resting) fluid, *tangential and normal motion* of a fluid with respect to the boundary, and a fluid *impacting a corner*. We propose ten experiments, comprising experimental setup and quantitative evaluation with optional visual inspections, that are arranged in four groups which focus on one of the main category of fluid-boundary interactions. We use these experiments to evaluate three particle-based boundary handling methods, that is, pressure mirroring, pressure boundaries, and moving least squares pressure extrapolation, in combination with two incompressible SPH fluid simulation methods, namely IISPH and DFSPH, to establish a quantifiable relation between different combinations of boundary handling with simulation approaches and the main categories of fluid-boundary interactions. Finally, we summarize all results in a rating table and show how our experiments can be used to determine the promising method for specific requirements regarding a given constellation of fluid-boundary interaction.

KEYWORDS

comparison, fluid simulation, method evaluation, smoothed particles hydrodynamics (SPH)

1 | INTRODUCTION

Along with the growing importance of fluid simulations within computer animation and computational fluid dynamics, various methods have been developed for boundary handling. In this article, we focus on smoothed particle hydrodynamics (SPH), one of the most popular methods for fluid simulation in computer animation. Initially, boundary handling methods predominantly focused on solving the basic issues of fluid-boundary coupling in SPH, for example, fluid particles penetrating boundaries[1,2] and uncontrollable adherence to boundary surfaces.[3-5] More recent research focuses on solving more nuanced, additional, fluid-boundary interactions problems, for example, ensuring that pressure gradient around boundaries are smooth.[6,7] However, the evaluation of each individual method generally only focuses on the effect under consideration. While some experiments are frequently used for comparisons, such as the dam break experiment, they are applied in a non-uniform way, for example, using different scales or fluid parameters.[8,9] Furthermore, specific experiments are often difficult to reproduce due to a lack of precise geometric and parametric definitions,[7,10] a utilization of a variety of additional simulation components such as fluid-air interactions,[11] and a general lack of freely availability of reference implementations.[6-8,10-13] Consequently, comparing approaches across a broad range of experiments is hardly possible as each individual method's set of evaluations is designed to highlight the specific method's benefits, although the method may exhibit shortcomings in other experiments that highlight other fluid effects. In contrast, computational fluid dynamics regularly utilizes standardized experiment test cases, for example, those provided by SPHERIC,[14] for a quantifiable comparison of the overall fluid behavior based either on analytical models or experimental data. However, these experiments generally involve complex setups[15,16] with interdependent fluid effects, which makes it difficult to evaluate individual fluid-boundary effects in isolation, for example, unwanted boundary resistance may be superimposed by fluid-boundary adhesion. Moreover, experimental data is commonly very limited in terms of spatial or temporal resolution, that is, fluid quantities are captured only in very few locations.[17] Another source of methods for evaluating fluid simulations is survey papers.[18,19] The evaluation provided in such papers usually includes only qualitative assessments of strengths and weaknesses of the methods, without quantitative analysis.

In our article, each individual experiment contains a comprehensive description of the experimental setup, including a definition of all relevant fluid parameters, and is based on a set of quantifiable metrics, for example, kinetic energy, velocity, and pressure distribution, with additional visual evaluation for some experiments. We use each of our experiment to evaluate three boundary handling approaches: (i) pressure mirroring (PM),[3] (II) pressure boundaries (PB),[7] and (iii) moving least squares pressure interpolation (MLS).[6] Furthermore, for each boundary handling approach we utilize two different SPH simulation techniques: (i) implicit incompressible SPH (IISPH),[20] and (ii) divergence-free SPH (DFSPH).[21] Finally, we utilize our set of experiments to establish a clear and quantifiable relationship between the quantities measured in each experiment and fluid-boundary interactions relevant in computer animation to provide a clear basis for the comparison of different fluid boundary handling methods. Our contribution in brief:

- A set of well-defined experiments for four constellations of fluid-boundary interactions.
- A set of quantitative evaluation protocols for our experiments.
- An application of experiments and evaluation protocols to three boundary handling methods, each using two incompressible SPH techniques.
- A quantifiable process to determine the most well-suited method for the simulation of fluid-boundary effects under specific conditions.

2 | RELATED WORK

Smoothed particles hydrodynamics (SPH) is a Lagrangian fluid simulation approach that was initially proposed by Gingold and Monaghan[22] for astrophysical phenomena. Boundary interaction in SPH is handled by either discretizing the boundary objects into Lagrangian particle-based representations,[3] or by using non-Lagrangian models directly, for example, integrating over signed distance fields.[23] While there are frequently used evaluation experiments applied in different papers, the evaluation of boundary handling methods in computer animation mainly relies on visual inspection, and often uses experiments specifically designed to assess the main benefits of the proposed method. Examples are the

filling of a vase[6] or complex boundary geometries like canyons[24,25] or boats.[3] Moreover, the frequently used experiments are not well standardized across different papers, and use, for example, different experiment scales, boundary sampling, or fluid parameters (surface tension, viscosity, or time stepping). For example, the dambreak experiment[17] is utilized by Crespo et al.[26] using a global CFL-based time-stepping scheme proposed by Monaghan and Kos,[27] while Lee et al.[28] use the method proposed by Morris et al.[29]

In the following, we briefly discuss the main purpose of some prominent, commonly used experiments. The widely used *dambreak experiment*[6,7,10,12,13,23,25,30-33] involves an initial fluid volume flowing into a larger simulation domain and potentially interacting with obstacles placed within the simulation. It is used for both the evaluation of fluid simulation techniques[1,8] and boundary handling methods.[13,25] This experiment is evaluated as a visual assessment of the overall fluid behavior,[12,32] for visual and quantitative comparisons[8,11] and for quantitative comparison[33] involving experimental SPHERIC data.[14] However, the setup of the experiment is altered in many ways. There are, for example, different sizes on the basin from 3 m long till tens of meters long[6,34] and of the initial fluid volume, for example, different shape and size of the fluid volume,[6,7,13] varying fluid parameters, for example, particle spacing and viscosity term,[23,31] and a varying number of obstacles, that is, no,[7,8,31] one,[12] or multiple/complex objects.[13] Another widely used experiment is the *still water experiment*[3,7,12,35-37] used to investigate the fluid behavior in a steady state. In this experiment, a fluid volume is generally placed in a simple simulation domain in a state that should not exhibit any fluid motions, for example, oscillations in the fluid surface. Different properties are analyzed in this experiment, for example, the average pressure,[7] the kinetic energy[7] or the pressure/velocity profile at the boundary/in bulk.[3,7,12] The geometric setup of the experiment differs significantly between different methods, for example, the simulation domain may be 2D[12,32] or 3D,[23,36] and use an orthogonal[7] or cylindrical[6] container. A third commonly used experiment is the *sliding plane experiment*, which is used to assess the fluid-boundary interaction in SPH, where a set of fluid particles is sliding down a tilted planar boundary surface.[3,13,21,25] The angle of the tilt[3,13] as well as the initial fluid configuration[3,21] vary significantly, and the overall evaluation usually involves assessing particle trajectories or any potential adhesion of particles to the boundary surface.

There are some prior publications that compare different fluid simulation techniques quantitatively and qualitatively with different objectives,[8,9,11,38,39] they do not explicitly evaluate the fluid-boundary interaction.

There are few prior works that provide explicit evaluations schemes for boundary-handling. Liu et al.[31] compare two fluid-boundary coupling methods originating from a CFD context, which are conceptually different from current state-of-the-art approaches used in computer animation. This evaluation is performed using a two-dimensional dambreak experiment and by investigating three different visual and quantitative evaluation approaches, that is, the fluid flow near the boundary, the fluid surface profile and back wave propagation. Sheikh et al.[40] consider boundary handling approaches used for simulating granular materials using SPH. They analyze numerous quantifiable aspects of experiments, for example, normal force, frictional force, and final deposit profiles of granular material.

In this article, we propose a set of experiments and quantitative as well as qualitative evaluation protocols specifically tuned for one-way coupled fluid-boundary interactions within a computer animation context. We, therefore, extend existing and introduce novel experiments and quantitative evaluation techniques. We provide full information of all experiments and quantitative evaluation protocols to ensure reproducibility. Specific differences between our proposed experiments and prior experiments, if applicable, are explained in more detail in corresponding experiment setup in Section 4.

3 | SPH BOUNDARY HANDLING METHODS

Boundary geometries in SPH are either treated directly, for example, using integral based formulations, or they are discretized into a Lagrangian form, yielding *particle-based boundary handling* approaches.

In this article, we focus on particle-based approaches, as this type of boundary handling is the most popular used in SPH. Due to consistent discretization of fluid and boundary geometry, integrating the fluid and the fluid-boundary solvers as well as solvers for external effects, for example, adhesion, is relatively easy and straightforward. However, this choice of discretization does not restrict the use of the proposed set of experiments to particle-based boundary handling methods, and it is possible to use our experiments and evaluation protocols for any non particle-based method as well.

Particle-based boundary handling methods either utilize surface sampled particles[3] or dense volume sampling of the boundary object,[1] where both samplings face several challenges regarding the placement of particles. Several approaches

have been developed to improve the generation of surface sampled particles,[41,42] however, all sampling strategies exhibit some artifacts, for example, non-perfectly smooth surfaces or fluid particle penetration due to inhomogeneous sampling. Due to their wide usage within computer animation, we focus on surface-sampled approaches. Moreover, we restrict the set of experiments to regularly shaped boundary objects without applying any sampling optimization for the sake of simplicity of implementation. The incorporation of boundary particles into the standard discretized SPH interpolation scheme to evaluate a quantity A at position $\mathbf{x}$ yields:[3]

$$A(\mathbf{x}) = \sum_j \frac{m_j}{\rho_j} A_j W(\mathbf{x} - \mathbf{x}_j, h) + \sum_b \frac{\psi_b}{\rho_b} A_b W(\mathbf{x} - \mathbf{x}_b, h), \tag{1}$$

where $\mathbf{x}_j$ is the position of particle j, m_j is the mass of particle j, ρ being the density, and $\psi_b = \rho_0 V_b$ is the volume dependent mass factor, with ρ_0 being the rest density of the boundary, and V_b being the rest volume of the boundary particle b.[3]

Evaluating pressure forces is achieved by computing the pressure gradient, ∇p, using a standard SPH formulation for the gradient,[7] which yields

$$F_i^p = -\frac{m_f}{\rho_f} \left(\sum_j \frac{m_j}{\rho_j} (p_f + p_j) \nabla W_{fj} + \sum_b \frac{\psi_b}{\rho_b} (p_f + p_b) \nabla W_{fb} \right), \tag{2}$$

where F_i^p is the pressure force enacted upon the fluid particle i, which contains a summation over neighboring fluid particles j and neighboring boundary particles b.

Several approaches exist to evaluate the pressure values for boundary particles, where we evaluate three approaches due to their wide utilization in computer animation: *pressure mirroring*, *pressure boundaries*, and *moving least squares pressure extrapolation* (see Figure 1).

Pressure mirroring (PM) The underlying concept of PM is to set the pressure for a boundary particle to the pressure of the interacting fluid particle.[3] The pressure for all boundary particles is assumed to be equal to the fluid particle's pressure that is currently evaluating its pressure force, and, in general, every fluid particle evaluates a different pressure value for the same boundary particle (see Figure 1a).

Pressure boundaries (PB) Band et al.[7] apply an implicit SPH-like formulation to estimate unique pressure values for boundary particles within the SPH simulation process. They use a discretization of the pressure Poisson equation, resulting in a system of equations that is solved using a relaxed Jacobi method.

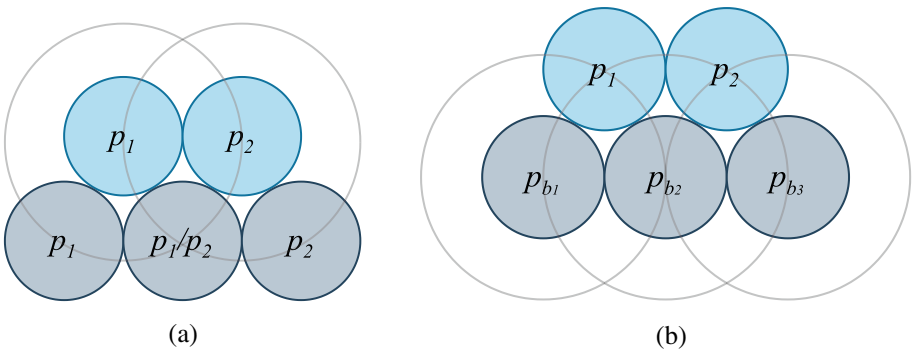

FIGURE 1 Boundary pressure methods involving boundary samples (gray) and fluid samples (blue). *Pressure mirroring* leads to different boundary pressure values, as different fluid particles project their pressure value to the same boundary sample, for example, in (a) the central boundary particle has pressure values p_1 or p_2, depending on whether it is evaluated from particle 1 or 2, respectively. *Pressure boundaries* and *moving least squares pressure interpolation* estimates a unique pressure value for each boundary particle using a pressure Poisson equation or extrapolates fluid particles' pressure onto boundary particles, respectively (b). (a) Pressure mirroring; (b) pressure boundaries, MLS

Moving least squares pressure extrapolation (MLS) This approach employs a moving least squares technique to calculate the pressure at boundary particles.[6] The moving least squares method is used to compute hyperplanes in the spatial-pressure domain that is used to estimate the pressure field at the considered boundary particle. The resulting pressure distribution extrapolates pressure to boundary particles, and the obtained pressure gradients are continuous.

4 | TESTING EXPERIMENTS AND RESULTS

We propose a set of ten experiments to examine specific boundary handling aspects. The schematic structures of the experiments are presented in Figure 2. Our ten experiments are arranged in four groups that evaluate four different categories of fluid-boundary interactions that are relevant to computer animation:

No motion: Even in the case of a *resting fluid*, any inconsistent or volatile physical quantities delivered by the boundary handling has an effect on the fluid that may lead to an unsteady fluid and *residual fluid motion*. This is mainly evaluated in Section 4.2.

Tangential motion: The boundary representation and handling has a significant impact on the behavior of a fluid under tangential motion.

One aspect refers to *artificial surface roughness*, also referred to as bumpiness, that describes the deviation of the perfect linear motion of the fluid along a planar surface by introducing motion in Z-direction. The artificial surface roughness mainly relates to the boundary discretization using particles,[6,13,23,25] which yields visible artifacts, such as particles moving along deflected paths.

A second aspect refers to *artificial boundary anisotropy*, that is, tangential motion of the fluid that directionally depends on underlying boundary representation. For instance, this effect may result in fluid particles moving preferably along the cardinal directions of a regularly sampled boundary.

A third aspect refers to an *unwanted artificial resistance* that occurs during interaction between particles due to underlying numerical effects and surface geometry. While this effect may correlate with artificial surface roughness, it results from a combination of fluid-fluid and fluid-boundary interaction and affects motion in XY-direction only. It is important to note that this effect works in addition to any boundary conditions, that is, no-slip or free-slip boundaries, and is significantly more apparent for free-slip boundaries, which are commonly used in computer animation.

These aspects are mainly evaluated in Section 4.3.

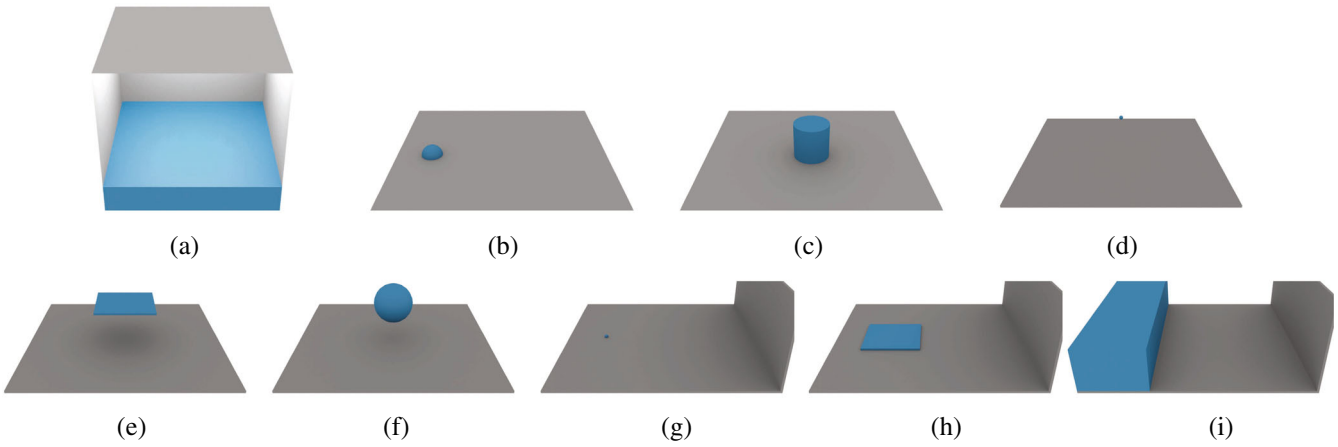

FIGURE 2 Schematic structure of the ten experiments used for four SPH experiments

Normal motion and impact: The boundary handling affects the fluid's behavior in vertical direction and may lead to an *artificial boundary elasticity*, where fluid particles impacting the boundary are bouncing away from the boundary surface instead of having no orthogonal velocity relative to the boundary normal. This is mainly evaluated in Section 4.4.

Corner motion and impact: Due to the smoothing property of SPH, the fluid-boundary interaction at sharp corners, where tangential and normal fluid components highly interact might lead to a *corner smoothing effect*. This effect is inherent to SPH and applies to smaller features as well.[25] It, however, also depends on the boundary representation, which is mainly evaluated in Section 4.5.

Our proposed experiments are constructed to investigate these categories in an as isolated way as possible, utilizing specific quantifiable evaluations. Some of the experiments are inspired by prior work. These aspects will be detailed in the specific experiment sections. After introducing technical preliminaries in Section 4.1, we describe in detail the four groups of experiments comprising ten experiments and the quantitative evaluation protocols. We evaluate the results obtained from our experiments in the aggregated rating Table 8.

4.1 | Technical preliminaries

4.1.1 | Simulation environment

As the environment for the evaluation we use the GPU-based open source SPH framework openMaelstrom.[43] Artificial viscosity to ensure stable fluid-fluid interaction is modeled based on the XSPH approach by Monaghan,[44] with viscosity coefficient $\alpha = .05$. Surface tension effects are modeled using the method by Akinci,[45] with a tension coefficient of $\kappa = .125$. As kernel function we utilize the cubic spline kernel[44] for all SPH evaluations besides the pressure gradient terms, where we use the spiky kernel[2] to avoid particle pairing instabilities. The gravity is set to $(0, 0, -9.8)^\top$ m/s^2, unless otherwise specified. Fluid particles and rigid particles have a radius of .05 m. Boundary sampling is regular rectangular with the spacing of .08 m. The density of the fluid and the rigid objects is set to 1000 kg/m^3. The time step during simulations is fixed at 1 ms, which satisfies the CFL condition for any simulation performed during our experiments. The stopping criteria for fluid solvers in all experiments is a average density error of .01%, for IISPH and DFSPH, and a average divergence error of .1% for DFSPH. For our comparisons, we implemented the boundary pressure terms PM,[3] PB,[7] and MLS,[6] and combine them with the IISPH[20] and DFSPH[21] fluid pressure solvers.

4.1.2 | Relaxation stopping criterion

Setting up an initial, relaxed fluid volume is a crucial aspect that strictly depends on a relaxation stopping criterion. We employ a relaxation stopping criterion purely based on the velocity magnitude $v_i(t)$ of particle i at simulation time t with time steps of $\Delta_t = 1$ ms. We define the average velocity magnitude per simulation time step $v_{\text{avg}}(t)$, and the average velocity magnitude over five seconds of simulation $v^{5\text{s}}_{\text{avg}}(t)$.

$$v_{\text{avg}}(t) = \frac{1}{n}\sum_{i=1}^{n} v_i(t), \qquad v^{5\text{s}}_{\text{avg}}(t) = \frac{1}{5000}\sum_{j=0}^{4999} v_{\text{avg}}(t - j \cdot \Delta_t),$$

where n is the number of fluid particles. The stopping criterion relates to the relative change of average velocity over 5 s simulation time within 1 s, that is:

$$\overline{v^{5s}_{\text{avg}}}(t) = (v^{5\text{s}}_{\text{avg}}(t) - v^{5\text{s}}_{\text{avg}}(t-1))/v^{5\text{s}}_{\text{avg}}(t-1). \tag{3}$$

Now we define the criteria to stop the relaxation at time t_0 if

$$\overline{v^{5s}_{\text{avg}}}(t_0 - \tau) < \delta, \forall \tau \in [0, 5] \text{ s}, \tag{4}$$

where δ is threshold, which in all our simulations is set to .05. In rare cases of high unsteadiness of the fluid, we stop at $t_0 = 300$ s.

We use the stopping criteria in all experiments where a relaxation of the fluid is necessary prior to executing the actual experiment and/or prior to measuring the quantitative values.

4.1.3 | Simulation hardware

All evaluations have been performed on an Intel Core i7-7700 CPU with 16 GB of RAM and an NVIDIA 2080ti GPU with 11 GB of VRAM.

4.2 | No motion experiments

In this group of experiments, we focus on the *no motion* category of fluid-boundary interactions.

This group of experiments consists of a fluid placed on a boundary plane or in a container in order to relax, that is, get to a resting state (see Figure 2a). Investigating resting fluid volumes has been done in prior work by Akinci et al.,[3] Band et al.,[7] Monaghan et al.,[35] and Mayrhofer et al.[36] Within this prior work there is no unified evaluation strategy, for example, Monaghan and Kajtar[35] measure pressure at the middle point of the container, while Band et al.[7] measure average pressure of the overall fluid and the total kinetic energy. We extend this approach by using additional fluid configurations, that is, a single particle and fluid sheets, and by having more versatile evaluations.

4.2.1 | Simulation setup

This group of experiments comprises two distinct experiments. The first experiment has three variants of fluid particle configurations, that is, a single fluid particle and a single layer fluid sheet comprising a single fluid particle surrounded by a hexagonal ring of 6 fluid particles or surrounded by two hexagonal rings of fluid particles with 18 fluid particles (see Figure 3). The fluid is placed onto a horizontal boundary plane (see Figure 2b) and is simulated until it fulfills the stopping criterion in Equation (4). The evaluation uses the simulation results up until the fluid fulfills the stopping criterion.

The second experiment consists of a boundary container with interior size of $1.0 \times 1.0 \times 20.0$ m^3 and a $.75 \times .75 \times 10.0$ m^3 fluid volume placed inside consisting of 1478 fluid particles. With a particle volume of $(2r)^3$,[7] the volume of the fluid amounts to 1.478 m^3. In this experiment, we use the maximum pressure, defined by the hydrostatic pressure, in the given container $p_{\max} = \rho \cdot g \cdot h = 1000 \cdot 9.8 \cdot 1.478 = 14484.4$ Pa[46] as a reference, and the pressure should ideally be uniformly distributed over $[0, 14484.4]$ Pa. In this experiment, initially, the fluid volume is positioned 5 particle radii

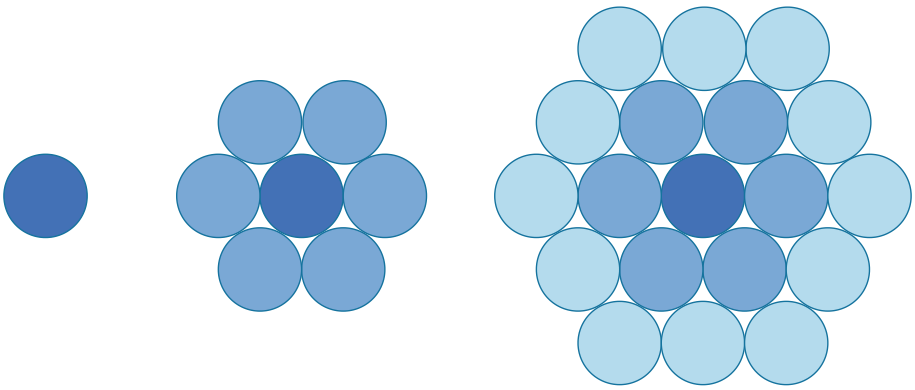

FIGURE 3 No motion experiments, planar particle sets. A single fluid particle (dark blue), a single fluid particle with one ring of neighbors (blue), and a single fluid particle with two rings of neighbors (light blue).

away from the container's bottom and side, that is, the fluid volume initially drops into the container without any initial fluid-boundary interaction. The fluid is simulated until the stopping criterion in Equation (4) is fulfilled. After the stopping criterion is met, the fluid is simulated for a further 10 s. Accordingly, any measurements for the second experiment include a residual influence of the initialization process, and we observe this residual influence and overall behavior for the last 10 s of the simulation.

4.2.2 | Evaluation protocol

In the first experiment, all tracked values are used as a measure for *residual fluid motion*. We track the *average relative tangential displacement*:

$$D^{\text{rel}}(t) = \frac{1}{n}\sum_{i=0}^{n}\left|\left|p_i^{xy}(t) - p_i^{xy}(0)\right|\right|, \tag{5}$$

where $p_i^{xy}(t)$ is a tangential position of the fluid particle i at time t, p_c^{xy} is the initial center of gravity of the fluid particles, and n is the number of particles in the configuration. Note, that $D^{\text{rel}}(t)$ would be 0 for an ideal surface. We also track the *average relative fluid height*:

$$H^{\text{rel}}(t) = \left(\sum_{i=0}^{n}(p_i^z(t))/n\right) - z_0, \tag{6}$$

where p_i^z is Z-coordinate of the fluid particle i and z_0 is the average particle height over all particles and time frames. Finally, we track the *average kinetic energy*:

$$E_k^{\text{avg}}(t) = \left(\sum_{i=0}^{n}\frac{m_i v_i^2(t)}{2}\right)/n, \tag{7}$$

where m_i and v_i is mass and the velocity magnitude of the fluid particle i, respectively.

The property assessed in the second experiment is the same *residual fluid motion*, but here we investigate a bulk fluid. For this purpose, we track the velocity and the pressure of all fluid particles over time to capture the detailed spatial-temporal fluid behavior. To get an overview, we aggregate this data in 2D histograms, showing the distribution of each quantity over time during the evaluation period. We evaluate these 2D histograms separately for particles in close proximity to the boundary, that is, particles that are less than 1.5× support radii away from the boundary, and for particles in the fluid's bulk. However, we also use aggregated values for a cumulative comparison between methods. To this extent, we calculate standard deviation of the 95% percentile over time for pressure and velocity. We also use the Wasserstein distance[47] to calculate the deviation of the pressure distribution from the ideal one, which is the linear increase from 0 to $p_{\max}$ proportional to fluid depth.

4.2.3 | Results

The results for the first experiment are presented in Figure 4 and Table 1 (the table is used in our rating scheme; see Table 8). The first, second, and third row in Figure 4 show the relative average tangential displacement, the relative average height, and the average kinetic energy for 0, 1, and 2 neighbors, respectively. The values for the relative height are presented in log-scale to show variations at lower scales. To prevent none-positive values for the log-scale, the results were shifted by overall minimum of the relative height plus a threshold. The results for MLS and PM for the single particle configuration are identical. The reason is that MLS for single particle degenerates to PM in its formulation (see Appendix Section 2). Although there are differences between PM and MLS for multi particle configurations, both methods tend to produce very similar measures.

For the single particle configuration, PM and MLS exhibit notable oscillations of the relative displacement (see Figure 4). Frequency and amplitude of the oscillation changes significantly, that is, the frequency decreases while the

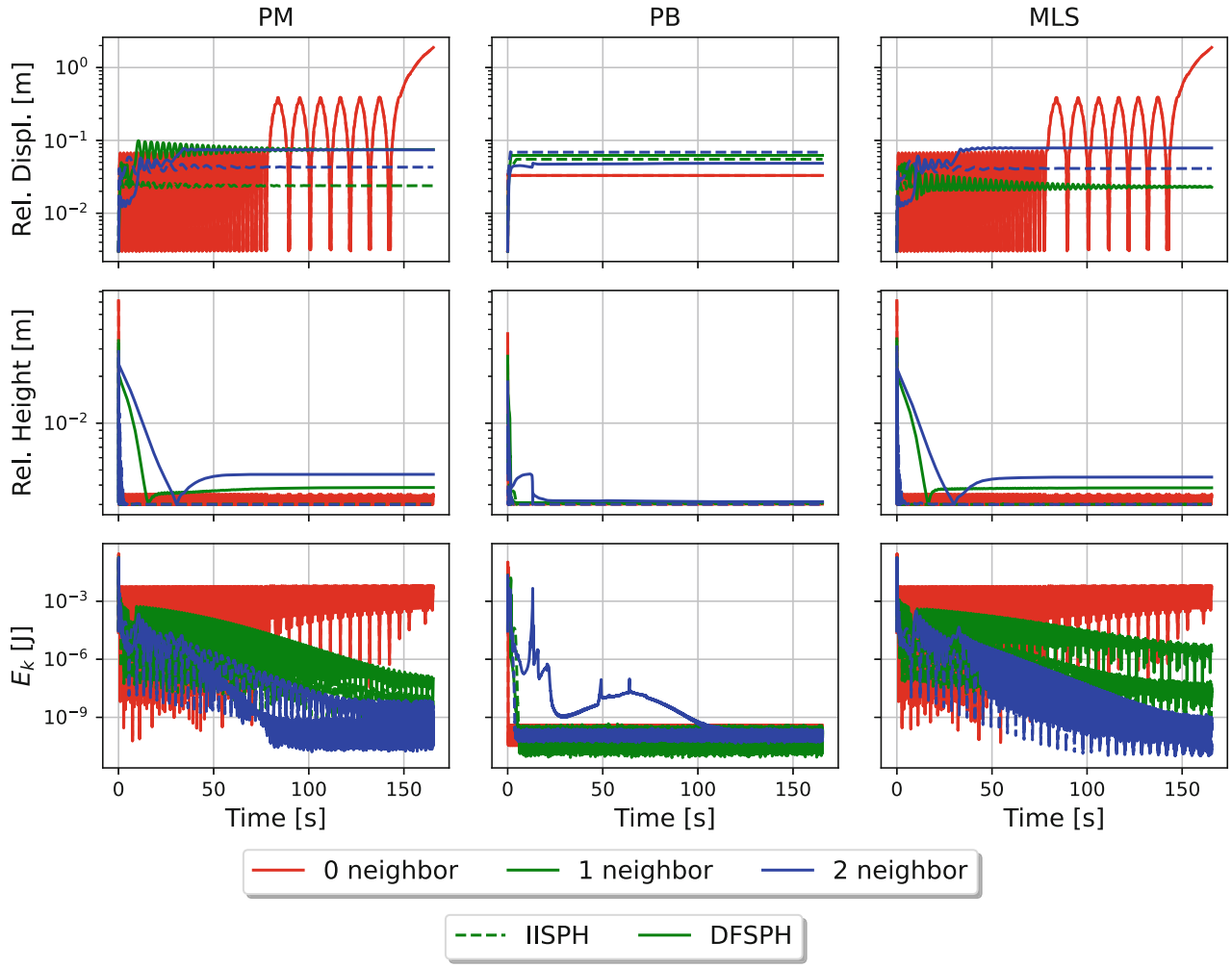

FIGURE 4 No motion experiments, planar particle sets. The relative fluid height and relative kinetic energy.

TABLE 1 No motion set of experiments, planar sets of fluid particles.

Par.	Neigb.	Stats.	PM+IISPH	PM+DFSPH	PB+IISPH	PB+DFSPH	MLS+IISPH	MLS+DFSPH
Rel. displacement	0	μ	1.83e+00	1.83e+00	3.00e-02	3.00e-02	1.84e+00	1.84e+00
		σ	2.15e-02	2.15e-02	9.11e-09	9.11e-09	2.17e-02	2.17e-02
	1	μ	2.09e-02	7.20e-02	5.22e-02	5.92e-02	2.00e-02	2.02e-02
		σ	9.11e-06	3.73e-05	5.66e-09	1.28e-08	9.81e-06	2.10e-04
	2	μ	3.99e-02	7.11e-02	6.59e-02	4.55e-02	3.81e-02	7.56e-02
		σ	1.53e-06	7.38e-07	4.53e-09	1.82e-08	2.08e-07	2.79e-06
Rel. height	0	μ	2.70e-04	2.70e-04	4.90e-09	4.90e-09	2.68e-04	2.68e-04
		σ	1.27e-04	1.27e-04	3.73e-09	3.73e-09	1.26e-04	1.26e-04
	1	μ	1.72e-08	5.74e-08	2.04e-09	6.60e-09	1.95e-07	4.70e-07
		σ	1.29e-08	2.58e-08	1.51e-09	4.27e-09	1.55e-07	3.65e-07
	2	μ	3.90e-08	6.37e-08	2.10e-09	1.83e-09	4.05e-09	9.03e-08
		σ	3.11e-08	4.67e-08	1.58e-09	1.43e-09	3.08e-09	4.39e-08
Kin. energy	0	μ	2.59e-03	2.59e-03	1.34e-10	1.34e-10	2.56e-03	2.56e-03
		σ	2.18e-03	2.18e-03	1.07e-10	1.07e-10	2.13e-03	2.13e-03
	1	μ	7.14e-09	6.26e-08	7.90e-11	1.63e-10	2.41e-08	2.89e-06
		σ	4.40e-09	4.36e-08	3.92e-11	4.66e-11	1.25e-08	1.94e-06
	2	μ	1.81e-09	1.63e-10	1.26e-10	1.15e-10	2.77e-11	3.16e-10
		σ	1.02e-09	1.08e-10	2.80e-11	2.23e-11	9.54e-12	1.57e-10

Note: Mean and standard deviation of the relative displacement, relative height and the kinetic energy. Blue colored values are the best values in current row.

amplitude increases over time. Over the full 160 s simulation sequence presented in Figure 4 the frequency and the amplitude of the oscillation change significantly three times. For all other particle settings the oscillations disappear after some time. Moreover, the standard deviation decreases with increase of particle number (see Table 1). Unlike PM and MLS, PB shows the least oscillations for the relative displacement for all particle configurations and unlike PM and MLS reaches its equilibrium quickly.

Similar to the relative displacement, the relative height oscillates noticeably and at high frequency for the single particle configuration for PM and MLS (see Figure 4). For the multi particle configurations there are only minor height oscillations after the relaxation. For PB we have a low level of oscillation which is also reflected in the low standard deviation in Table 1. As an additional note, for DFSPH the relative height is larger than for IISPH when combined with PM and MLS. For PB the relative height is very similar for all particle configurations and for both solvers, that is, DFSPH and IISPH.

For all methods and all particles configurations notable kinetic energy oscillations occur. However, PB shows the least oscillation amplitudes and the least variance of the kinetic energy level for all particle settings, see Table 1. Unlike PB, PM and MLS exhibit a decrease of the kinetic energy in average with increasing number of fluid particles.

For all methods, an increasing number of particles in the setting usually produces less standard deviation and a lower mean values in all three fluid measures (see Table 1).

The results for the second experiment are presented in Figure 5 and Table 2 (the table is used in our rating scheme 8). MLS for both IISPH and DFSPH shows the smoothest and most uniform pressure for both, in bulk and at the boundary. The average Wasserstein distance between the ideal uniform distribution and the MLS pressure distribution is the

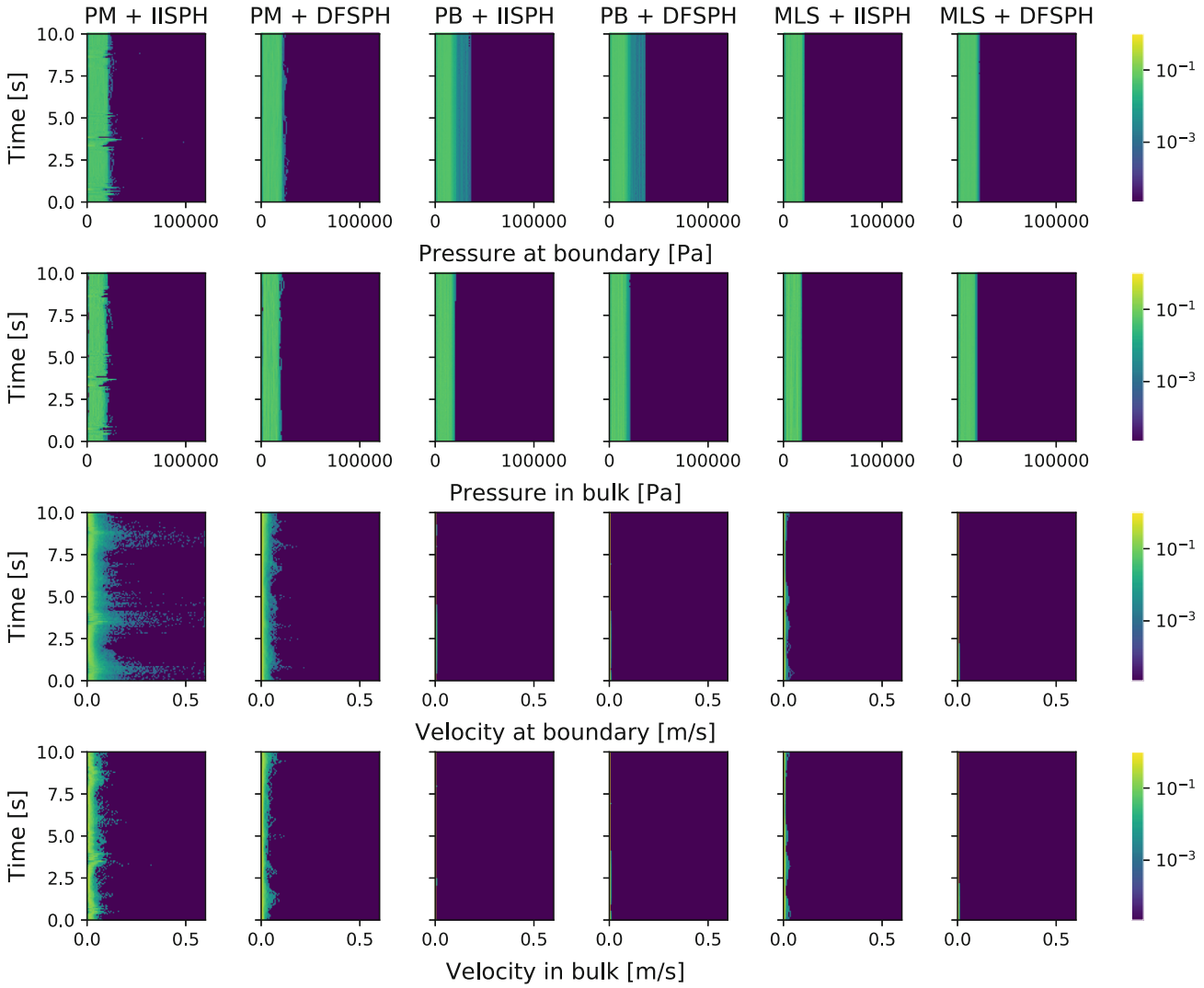

FIGURE 5 No motion experiments. Residual pressure and residual velocity in bulk and at boundary of the fluid.

TABLE 2 No motion experiments. The average Wasserstein distance ($\mathcal{W}_2(p)$) for all fluid particles over time, the standard deviation of the max. pressure σ_p in bulk and at the boundary, and the standard deviation of the max. velocity σ_v in bulk and at the boundary.

Stats.	Location	PM+IISPH	PM+DFSPH	PB+IISPH	PB+DFSPH	MLS+IISPH	MLS+DFSPH
$+\mathcal{W}_2(p)$	Whole	3.75e+03	3.57e+03	3.48e+03	3.53e+03	3.19e+03	3.08e+03
σ_p	Boundary	6.75e+03	1.33e+03	2.69e+01	5.31e+01	8.89e+01	2.48e+01
	Bulk	2.79e+03	1.08e+03	1.83e+02	1.36e+02	1.06e+02	2.02e+01
σ_v	Boundary	3.45e-01	3.05e-02	2.54e-03	1.58e-03	8.24e-03	2.66e-03
	Bulk	3.71e-02	2.02e-02	7.21e-04	1.51e-03	7.19e-03	3.14e-03

Note: Blue colored values are the best values in current row.

least among all given methods. The largest average Wasserstein distance for the pressure distribution is produced by PM+IISPH. The highest standard deviation for pressure is shown by PM+IISPH and the lowest is shown by MLS+DFSPH. For MLS, the lowest pressure deviation is expected due to definition of MLS, where boundary pressure continues pressure gradients smoothly, which is also declared in original work.[6] The standard deviation of velocity is the lowest for PB+DFSPH and the highest for PM+IISPH.

Conclusions

In the first experiment the ideal case is minor residual motion after relaxation, however MLS and PM preserve notable residual motion after relaxation and behave identical for the single-particle configuration and similar for the multi-particle configurations. PB shows better consistency with the ideal case.

For the second experiment, in the ideal case, the pressure distribution is uniform, as defined by the hydrostatic pressure. Overall, that is, considering the bulk and the boundary region, MLS for both IISPH and DFSPH shows the closest distribution to the ideal distribution. Similarly, MLS shows the smallest pressure standard deviation. However, for the velocity the lowest standard deviation is shown by PB. Comparing IISPH and DFSPH, DFSPH usually exhibits lower pressure and velocity errors, even though there are some exceptions, for example, Wasserstein distance for PB and standard deviation for PB in bulk.

4.3 | Tangential motion experiments

This group of experiments investigates the *tangential motion* of the fluid along a planar boundary surface. The main goal of the experiment presented here is to measure the *unwanted artificial resistance*, the *artificial surface roughness*, and the *artificial boundary anisotropy* that affects the fluid flow across the boundary surface.

This group of experiments comprises a boundary plane and different fluid particle configurations flowing over the plane (see Figure 2b,c). The group of experiments consists of two experiments with different setups and purposes:

1. The first experiment focuses on the *boundary surface roughness* and *unwanted artificial resistance*. The principal idea is based on works by Akinci et al.,[3] Koschier et al.,[23] Band et al.,[13] and Bender et al.[30] It comprises a regularly sampled plane and a moving configuration of fluid particles. Contrary to the prior works, we utilize a horizontal plane where we artificially accelerate the fluid particles instead of relying on gravity.
2. The second experiment focuses on the *artificial boundary surface roughness* and *boundary isotropy*, where the principal idea is based on works by Band et al.[6] and Bahman and Tong.[40] It comprises a fluid cylinder released on a regularly sampled plane. However, we utilize fluid instead of granular materials,[40] and do not place an obstacle in the path of the spreading liquid[6] to prevent additional fluid-boundary effects.

4.3.1 | Simulation setup

The first experiment consists of a horizontal boundary plane and a planar set of fluid particles (see Figure 2b). We use the same three variants of fluid particle configurations as from Section 4.2.

Prior to the measurement, the initial fluid particle configuration is simulated until the relaxation stopping criterion (4) is met. Afterwards, the fluid particles are accelerated until the fluid reaches an average velocity of $1 \pm .01$ m/s using a

tangential acceleration of 10 m/s^2. Then the acceleration is stopped, and the measurements begins for the next 5 s of simulation.

The second experiment comprises 3876 fluid particles initially forming a fluid volume shaped in the form of a cylinder with radius 1 m (see Figure 2c). The fluid cylinder is released after the fluid meets the relaxation stopping criteria (4).

4.3.2 | Evaluation protocol

In the first experiment, we measure the *unwanted artificial roughness* by tracking the *average relative fluid height* $H^{\text{rel}}(t)$ (6) and we measure *unwanted artificial resistance* by tracking the *average kinetic energy* $E_k^{\text{avg}}(t)$ (7) of the fluid. For ranking purpose, we fit data for *average kinetic energy* to the exponential decay function $a \exp(b \cdot t)$ and calculate the b coefficient while setting $a = .25$. We assign a constant value to a to be consistent with theoretical kinetic energy for the given set of particles.

In the second experiment, we assess the distribution of the fluid particles within the first 2 s after releasing the fluid cylinder. We evaluate the particle distribution over the boundary surface to assess the *artificial boundary surface resistance* and the *artificial boundary anisotropy* by measuring the polar angle distribution after 2 s in a 1D histogram and the polar radius distribution of the fluid particles for the full evaluation period of 2 s in a 2D histogram. The polar angle distribution is built using 200 bins. This distribution is expected to be uniform with probability of .005 for each bin. We therefore calculate the standard deviation of the probabilities from angular distribution obtained in simulation with respect to ideal uniform probability of .005. We refer to this distribution as angular probability distribution.

4.3.3 | Results

The results of the the first experiment are presented in Figure 6 and Table 3, the latter showing the measures for a fitted exponential decay function for the kinetic energy.

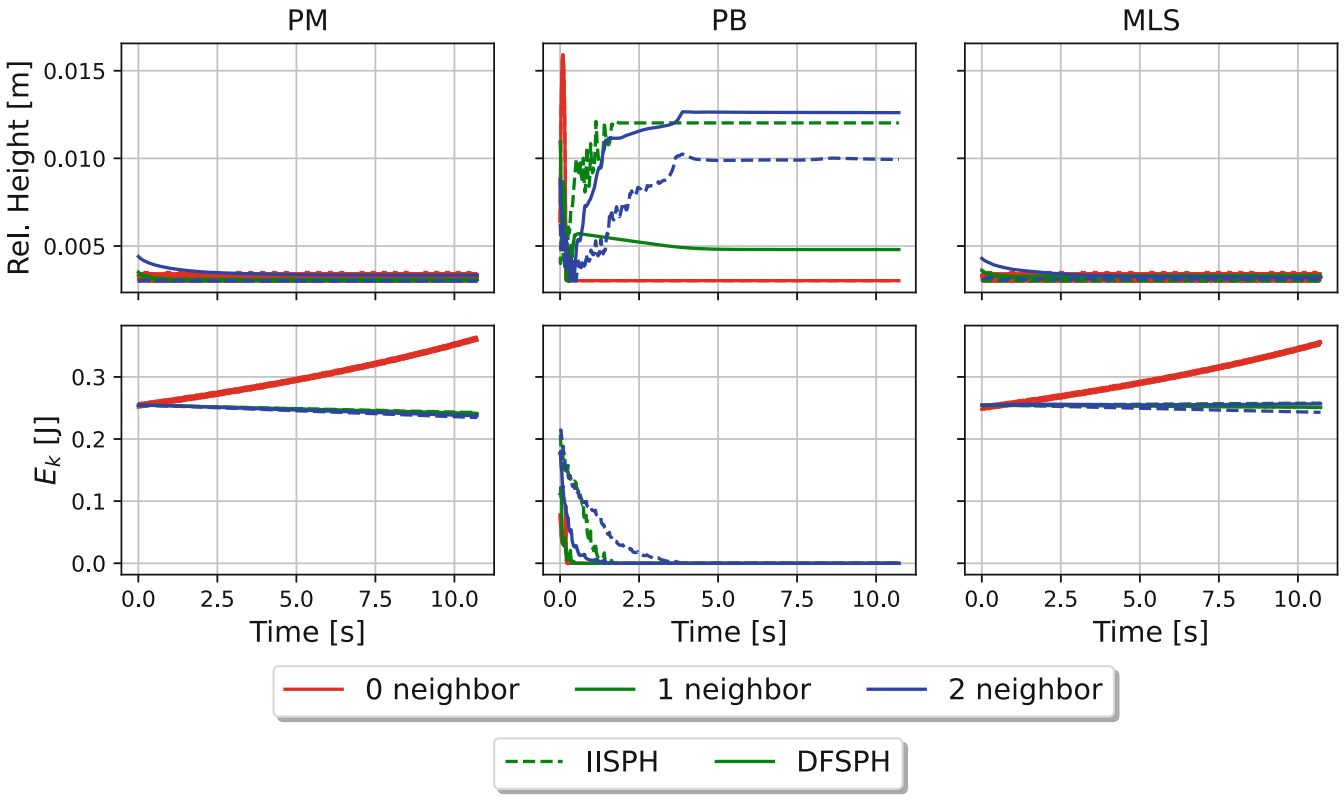

FIGURE 6 Tangential motion experiments, planar particle sets. The fluid relative height and average kinetic energy.

TABLE 3 Tangential motion experiments, planar sets of fluid particles.

Neihg.	Exp-fitting	PM+IISPH	PM+DFSPH	PB+IISPH	PB+DFSPH	MLS+IISPH	MLS+DFSPH
0	b	+3.39e-02	+3.39e-02	-1.40e+00	-1.40e+00	+3.15e-02	+3.15e-02
1	b	-2.03e-03	-2.46e-03	-1.84e+00	-2.49e+01	+3.61e-03	+1.17e-03
2	b	-4.90e-03	-3.86e-03	-1.21e-01	-5.82e+00	-1.65e-03	+3.13e-03

Note: Coefficient b of the fitting exponential decay function $a \exp(b \cdot t)$ for the kinetic energy.

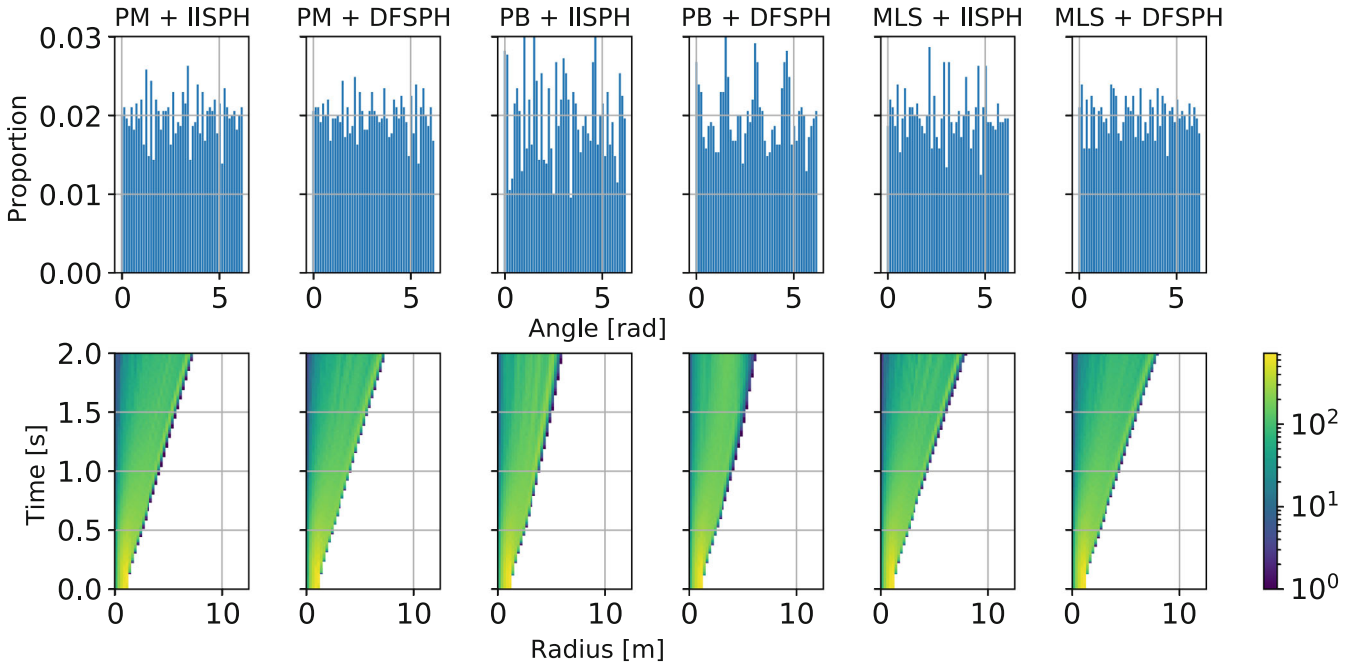

FIGURE 7 Tangential motion experiments, fluid cylinder. Polar angle distribution after 2 s of simulation (top row) and the polar radius distribution over 2 s after the cylinder barrel is released (bottom row).

Besides numerical variations, MLS and PM exhibit identical results for the single particle configuration, that is, the fluid particle accelerates even without external force. A similar anomaly, that is, a positive coefficient of the exponential function, occurs for MLS+IISPH with 1 ring of neighbors and MLS+DFSPH with 2 rings of neighbors (see Table 3). The highest deceleration occurs for PB, especially for combination with DFSPH, which is physically reasonable but unwanted because causes high artificial resistance. For higher numbers of fluid particles, the value of the fluid deceleration decreases for PB.

The results for the second experiment (fluid cylinder) are presented in Figures 7 and Table 4. Furthermore, we present a visual comparison of the fluid's shape after 2 s after the fluid cylinder barrel has been released in Figure 8. We observe that the fluid propagates much farther and quicker for the MLS and the PM method than for PB, which corresponds to the first experiment, where PB shows a high deceleration. Comparing MLS and PM, MLS exhibits a slightly farther particle propagation. According to Figure 7 and Table 4, PM and MLS in combination with DFSPH have a more uniform distribution and less standard deviation of the angular probability distribution (σ_{prob}) compared to the other combinations. PB exhibits a comparably strong anisotropy, that is, an angular dependency of motion, with a clear preference aligned with the boundary particles' grid axes when combined with DFSPH. However, the standard deviation of the angular probability distribution (σ_{prob}) for PB+IISPH is higher than for PB+DFSPH, which mainly results from clustering effects, that is, fluid particles unite in multiple clusters during the fluid spread. Additionally, cross-checking with the visual results in Figure 8, we can clearly see the lower artificial resistance for PM and MLS compared to PB. Moreover, we observe a difference regarding the fluid distribution between DFSPH and IISPH for PB.

TABLE 4 Tangential motion experiments, fluid cylinder.

Measure	Stats.	PM+IISPH	PM+DFSPH	PB+IISPH	PB+DFSPH	MLS+IISPH	MLS+DFSPH
Angular distr.	σ_{prob}	2.73e-03	2.35e-03	5.63e-03	4.13e-03	3.31e-03	2.34e-03
Radial distr.	μ	5.57e+00	5.62e+00	4.37e+00	4.30e+00	5.94e+00	6.07e+00
	σ	5.74e-02	5.86e-02	9.98e-02	1.96e-01	8.55e-02	8.59e-02

Note: Geometric distribution measures at 2 s of simulation. σ_{prob} is the standard deviation of the angular probability distribution. Blue colored values are the best values in current row.

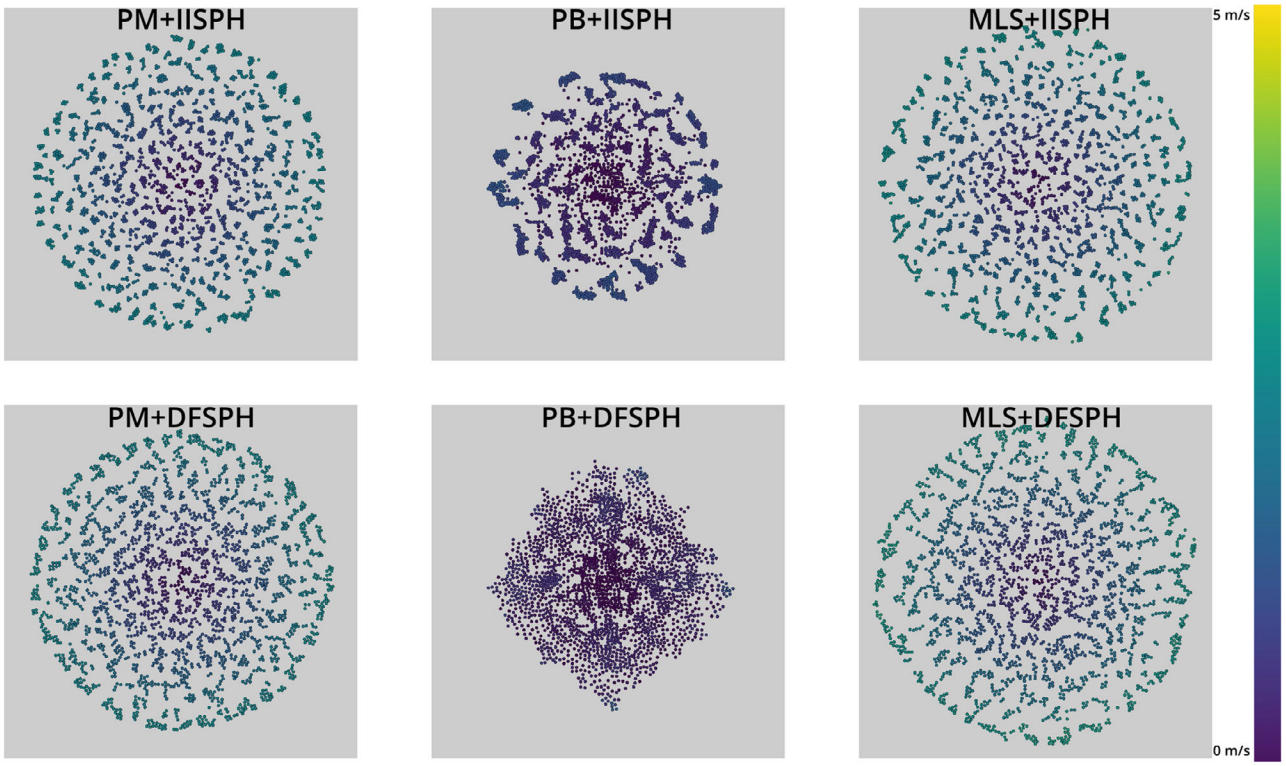

FIGURE 8 Tangential motion experiments, fluid cylinder. Top view 2 s after the cylinder is released.

Conclusions

PM and MLS show very similar behavior. They both show low artificial resistance or nonphysical artificial resistance for all particle configurations, as indicated by the the exponential decay b in Table 3. Consequently, in complex experiment, like the fluid cylinder, fluid particles are propagated further when using PM and MLS. The opposite result occurs for PB where the artificial resistance is very high, which stops the fluid quickly. This is good for the relaxation, but unwanted for the fluid flows.

4.4 | Normal motion experiments

In this group of experiments we investigate the *normal motion and impact* of fluid-boundary interactions by hitting a fluid with a planar boundary. The main goal of this experiment is to investigate *artificial boundary elasticity*, *artificial boundary anisotropy*, and *artificial boundary surface roughness* for varying fluid configurations. This group of experiments consists of a boundary plane aligned with the XY-plane and different fluid configurations perpendicularly impacting the boundary plane without the influence of gravity (see Figure 2d–f).

This group of experiments includes three experiments with different fluid configurations: a single fluid particle, a fluid sheet one particle thick, and a ball-shaped fluid volume.

4.4.1 | Simulation setup

Within the first experiment, we evaluate how a single particle impacts a boundary plane at different XY-positions and how this XY-position influences the particle-surface interaction. We place a single fluid particle initially at a distance of .3 m from the boundary plane in Z-direction and vary its XY-position. These positions are chosen to form a regular grid with 31×31 XY-positions that fully cover an area of 1×1 boundary particles, that is, the distance between neighboring XY-positions is 1/31 times the sampling distance of the boundary particles (see Figure 9a). The initial velocity of the fluid particle is set to 10 m/s towards the boundary plane. In this experiment, we track Z-component and XY-component of the fluid velocity. Moreover, we evaluate the velocity after boundary interaction as function of the XY-impact location, that is, we capture the particle velocity after there is no further interaction with any boundary particle, or 1 s after the simulation started, if the particle stays in interaction distance to the boundary plane. The ideal result would be that the particle stops at the location of impact.

In the second experiment, a fluid sheet aligned with the boundary plane is utilized that is $.7 \times .525$ m^2 in size and has a hexagonal grid structure with 37 fluid particles (see Figure 9b). The initial distance between the fluid sheet and the boundary plane is .3 m and its initial velocity is 10 m/s towards the boundary plane.

Finally, in the third experiment a fluid ball of radius of .5 m, consisting of 359 fluid particles in a hexagonal grid structure located at a distance of 1.3 m above the plane is utilized with an initial velocity of 10 m/s towards the boundary plane.

4.4.2 | Evaluation protocol

In the first experiment with a single fluid particle, we track the Z-velocity and the XY-velocity direction and magnitude. We visualize the XY-velocity and the Z-velocity magnitudes after boundary impact in a joint 2D visualization. Moreover, we extract aggregated values from the data: mean of $|v_z|$, max of $|v_z|$, mean of $|v_{xy}|$, max of $|v_{xy}|$ and average divergence[48] of $|v_{xy}|$ for all particle impacts. The mean and max of $|v_z|$ are evaluating the *artificial boundary elasticity*, mean and max $|v_{xy}|$ are used for evaluating the *artificial boundary isotropy* and *artificial boundary surface roughness*.

In the second and the third experiment, we track the average fluid Z-velocity and the average XY-velocity magnitudes of the fluid particles. For the evaluation of the *artificial boundary elasticity*, we use aggregated value of mean $|v_z|$ after impact.

4.4.3 | Results

The first experiment with a single fluid particle shows that the amplitude and the XY-direction of the particle's velocity after boundary interaction highly depends on the point of impact with the boundary, as well as on the boundary handling

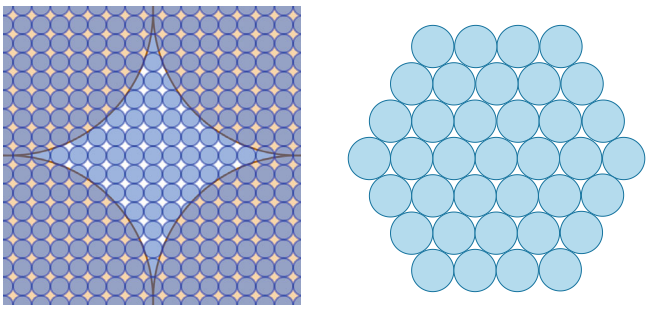

(a) (b)

FIGURE 9 Normal motion experiments, single particle. The grid (a) of fluid particle locations along XY-plane for the first experiment, that is, the single particle-boundary impact experiment. The large orange circles are boundary particle, the small blue circles are XY-locations at which the fluid particle impacts the boundary. And the configuration of the fluid sheet (b) used in the second experiment of the same experiment

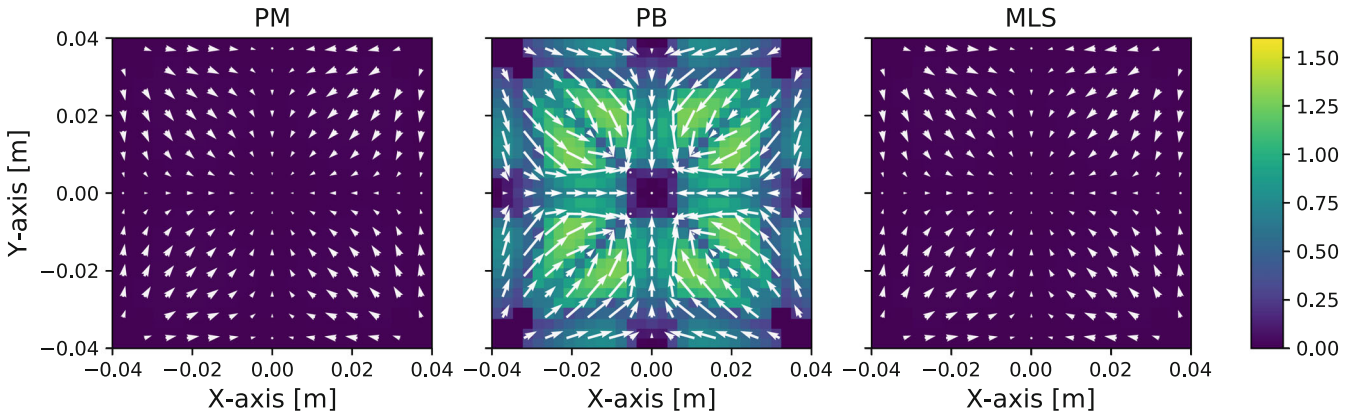

FIGURE 10 Normal motion experiments, single particle. Reflected particle velocity for the first experiment, that is, the single particle-boundary impact experiment. The color and the arrows encode the Z- the XY-component of the particle's velocity after boundary interaction, respectively.

TABLE 5 Normal motion experiments. Statistics of the single fluid particle-boundary impact experiment.

Stats.	PM	PB	MLS
$\mu(v_z)$	1.16e-02	6.83e-01	1.16e-02
max v_z	2.49e-02	1.28e+00	2.49e-02
$\mu(\|v_{xy}\|)$	5.46e-01	1.29e+00	5.46e-01
max $\|v_{xy}\|$	8.53e-01	2.30e+00	8.53e-01
Avg. $div(\|v_{xy}\|)$	2.39e-01	2.16e+00	2.39e-01

Note: Blue colored values are the best values in current row.

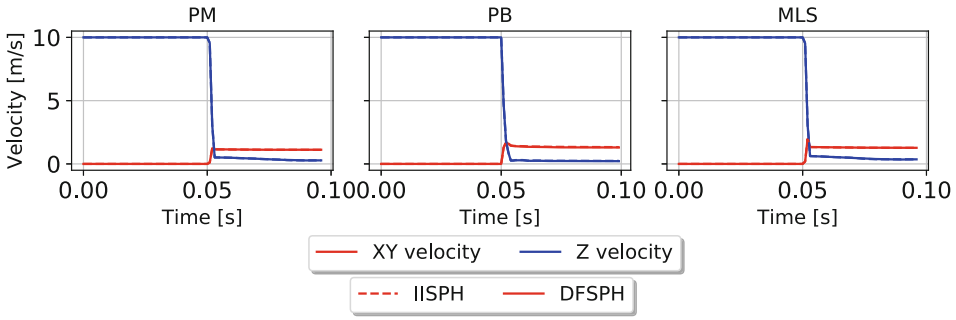

FIGURE 11 Normal motion experiments, fluid sheet. XY-vector and Z-components of the average fluid velocity for the fluid sheet-boundary impact experiment.

approach (see Figure 10). The results for PM and MLS are identical due to reasons described in the previous experiment (see Section 4.3). For some points, the reflection in Z-direction is almost zero and the maximal Z-velocity is 1.28 m/s (see Table 5). The highest magnitudes for the Z-velocity as well as for the XY-velocity are shown by PB. Similarly, the average divergence computed for the XY-velocity is significantly higher for PB than for PM and MLS.

The second experiment results are presented in Figure 11 and Table 6. After impact, the Z-component of the average velocity for PM and MLS is slightly higher than for PB. This result is not consistent with the result obtained for the single particle experiment, where PM and MLS show significantly lower Z-velocity, while PB exhibits a significant Z-velocity after impact. Interestingly, compared to PM and MLS, PB shows the least Z-velocity, while it exhibits the highest Z-velocity for the single particle experiment. The fluid simulation methods DFSPH and IISPH exhibit nearly identical results with a small difference in the mean Z-velocity for PB (see Table 6).

TABLE 6 Normal motion experiments. Mean v_z after impact for the sheet and the ball experiments

Experiment	Stats.	PM+IISPH	PM+DFSPH	PB+IISPH	PB+DFSPH	MLS+IISPH	MLS+DFSPH
Sheet	$\mu(v_z)$	.26	.26	.22	.20	.36	.36
Ball	$\mu(v_z)$	.55	.50	.93	1.00	.43	.43

Note: Blue colored values are the best values in current row.

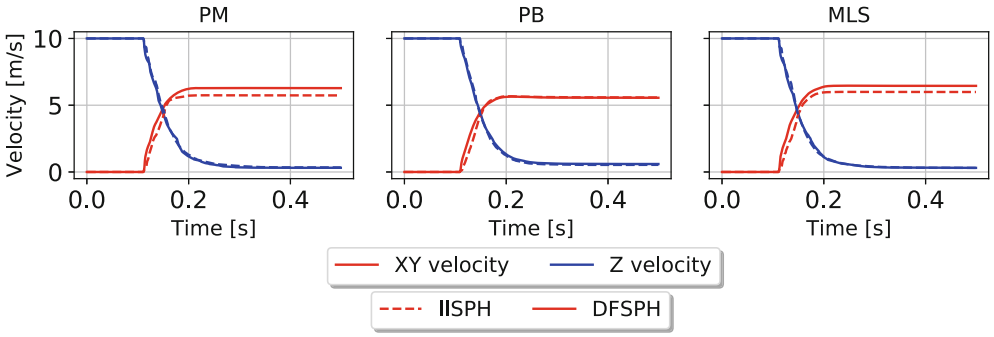

FIGURE 12 Normal motion experiments, fluid ball. XY-vector and Z-components of the average fluid velocity for the fluid ball-boundary impact experiment.

The fluid ball experiment's results are presented in Figure 12 and Table 6. In this experiment, PM and MLS show lower Z-velocities, which coincides with the results obtained single particle-boundary impact experiment. From Figure 12 we see that the average XY-velocity magnitudes for PM and MLS are slightly higher than for PB. Similar to the fluid sheet experiment, there is a small difference in the mean Z-velocity between IISPH and DFSPH in the fluid ball experiment (see Table 6), while there is a noticeable difference in the XY-velocity for PM and MLS.

Conclusions

Overall, PM and MLS deliver the lowest Z-velocity magnitudes for all experiments. For the single particle experiment, PM and MLS also exhibit a very uniform behavior compared to PB. Regarding the XY-velocity magnitudes, the PM and the MLS method also show the lowest values for the single particle experiment, while they exhibit the highest XY-velocity magnitudes for the fluid ball boundary impact. For the fluid sheet all three method show similar results. In general, we do not observe much difference between IISPH and DFSPH.

4.5 | Corner motion and impact experiments

We use this group of experiments to investigate the *corner motion and impact* of the fluid, focusing on the *corner smoothing effect*. We, therefore, simulate the impact of various fluid configurations with an orthogonal boundary concave corner (see Figure 2g–i), which has some experimental similarity to the well-known dambreak experiment.[17] Our experiment, however, quantitatively evaluates the behavior of various fluid configurations interacting with a boundary corner.

4.5.1 | Simulation setup

This group of experiments consists of three experiments. In the first experiment a single fluid particle is accelerated and impacts the orthogonal corner, where an XY- and a YZ-plane meet. The particle is initially located on the XY-plane and approaches the corner by moving in X-direction. The particle is accelerated until it reaches an average velocity of $1 \pm .01$ m/s before the impact. The analysed data is taken for .5 s before and .5 s during the time of impact. Ideally, the particle stops at the corner. The second experiment is a corner impact of a fluid sheet with 122 fluid particles that are accelerated and impact the corner. The impact takes place in the container with area of 1×2 m^2. The container is divided into two sections, each 1×1 m^2. The fluid sheet is placed in one of the sections and after fulfilling of the stopping criterion (4) the wall between sections is removed and the fluid sheet is accelerated to an average fluid particle velocity of

1 m/s with ±5 % precision with an acceleration of 10 m/s^2. We evaluate data for 2 s after the first impact of the sheet. The third experiment is a classical dambreak. The container used for this experiment has a ground plane of 4×12 m^2 which is divided into two sections with 4×4 m^2 and 4×8 m^2. The number of fluid particles is 113,189. Initially, the fluid stays in the smaller section of the container until it fulfills stopping criterion (4). Afterwards, the separating wall is removed and the released fluid flows towards the opposite wall. We evaluate 11 s after the dam release.

4.5.2 | Evaluation protocol

Evaluating the first experiment is done using 2D histograms for X- and Z-velocities. We also evaluate X- and Z-position over time. We take maximum v_z velocity due to the corner impact as indicator for the *corner smoothing effect*. For the second experiment the analysis of the obtained data is done using 2D time histograms for each velocity component. While we assess the corner impact (simulation time $1 - 3$ s), we also include .25 s before acceleration and .75 s of acceleration for completeness. In the graphs, the corner impact occurs at 1 s. For the evaluation of the *corner smoothing effect* we use the 95% percentile of v_z during corner impact. For the same simulation time we also calculate standard deviation of v_x and v_y. For the third experiment the analysis of the obtained data is done in 2D time histograms for each velocity component and includes 1 s before release and 11 s after release of the removal of the separating wall. For the evaluation we use the 95% percentile of v_z and v_x during whole simulation after dam release, the standard deviation of v_y and the v_x decay. The latter is calculated as ratio decay $= v_x1/v_x3$, where v_x1 is maximum v_x velocity before first impact and v_x3 the maximum v_x velocity between second and third impacts.

4.5.3 | Results

The result for the first experiment is presented in Figure 13. The particle behaves identically for PM and MLS as for previous single particle experiments Section 4.2. For PM and MLS, the velocity's X-component partially converts to a

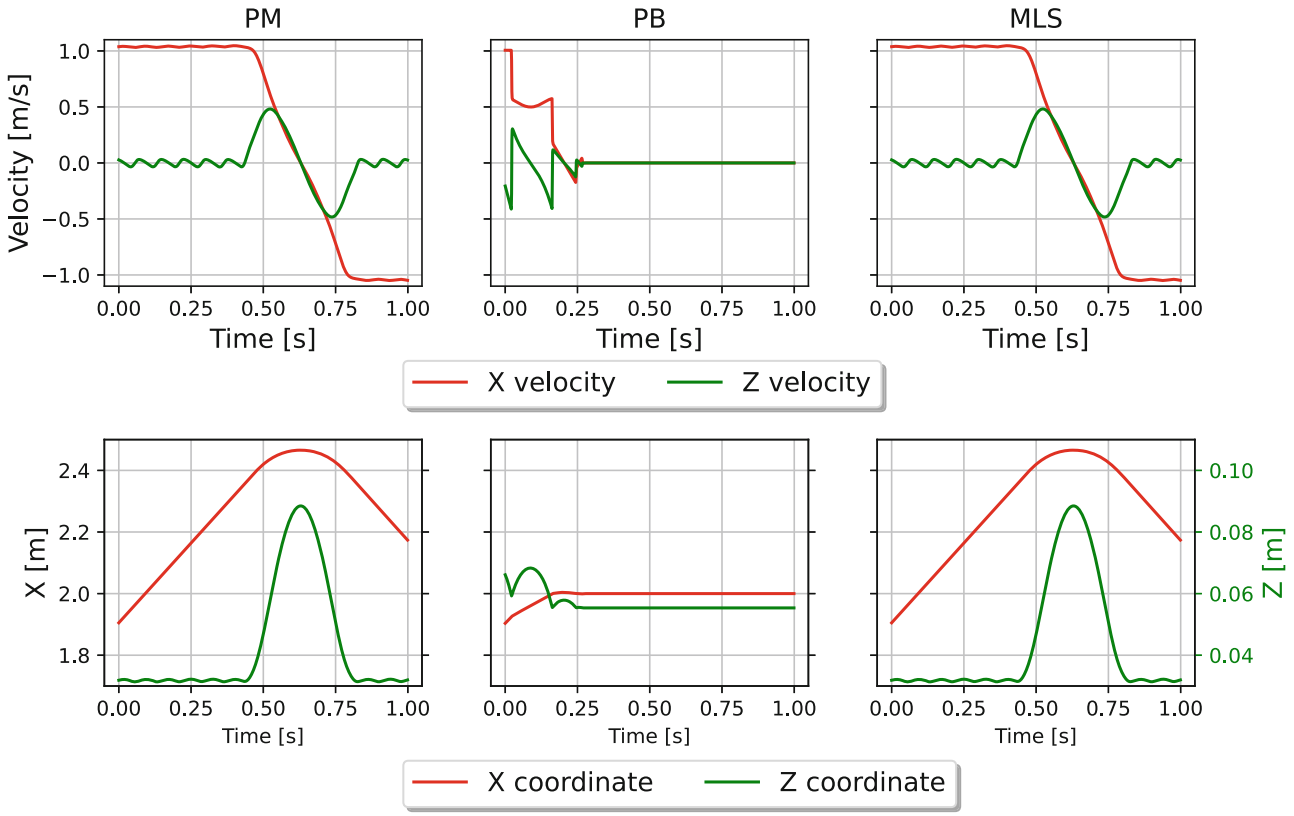

FIGURE 13 Corner motion and impact experiments, single particle. The X and Z components of the velocity (top row) and of the particle position over time (bottom row).

motion upward Z-velocity during the impact. After reaching the maximum height the fluid particle falls back but instead of sticking to the corner it moves backwards in X-direction. Visually it appears as if the corner is rounded. The maximum Z-velocity for PM and MLS is .482 m/s. For PB the velocity behaves differently. After the impact the fluid particle sticks close to the corner and oscillates for some time. The maximum Z-velocity for PB is .319 m/s, that is, smaller than for PM and MLS.

The second experiment's results are presented in Figure 14 and Table 7. The results are consistent with the results for the experiment with a single fluid particle, that is, PM and MLS show higher Z-velocity magnitudes than PB. This can be seen both, in Figure 14, last row, and in Table 7 for the 95% percentile v_z after the corner impact. The standard deviation of v_x during impact is higher for PM and MLS, whereas PB exhibits a lower deviation (see Table 7). The average standard deviation of v_y does not exhibit large differences for IISPH, however, for DFSPH, although PM and MLS have very similar values, PB shows lower variation.

The results for the last experiment, that is, the dambreak, are presented in Figures 15–17, as well as in Table 7. The first impact has the maximum X-velocity and happens around 2.5 s. The results include three wave impacts: first forward wave after dam release (happens at about 2.25 s), first backward wave (happens at about 4.5 s) and the second forward wave (happens at about 10 s). The 2D histogram in Figure 15 and the per-frame statistics in Figure 16, as well as the visual results in Figure 17 and the values in Table 7 exhibit, that, consistent with the prior experiments,

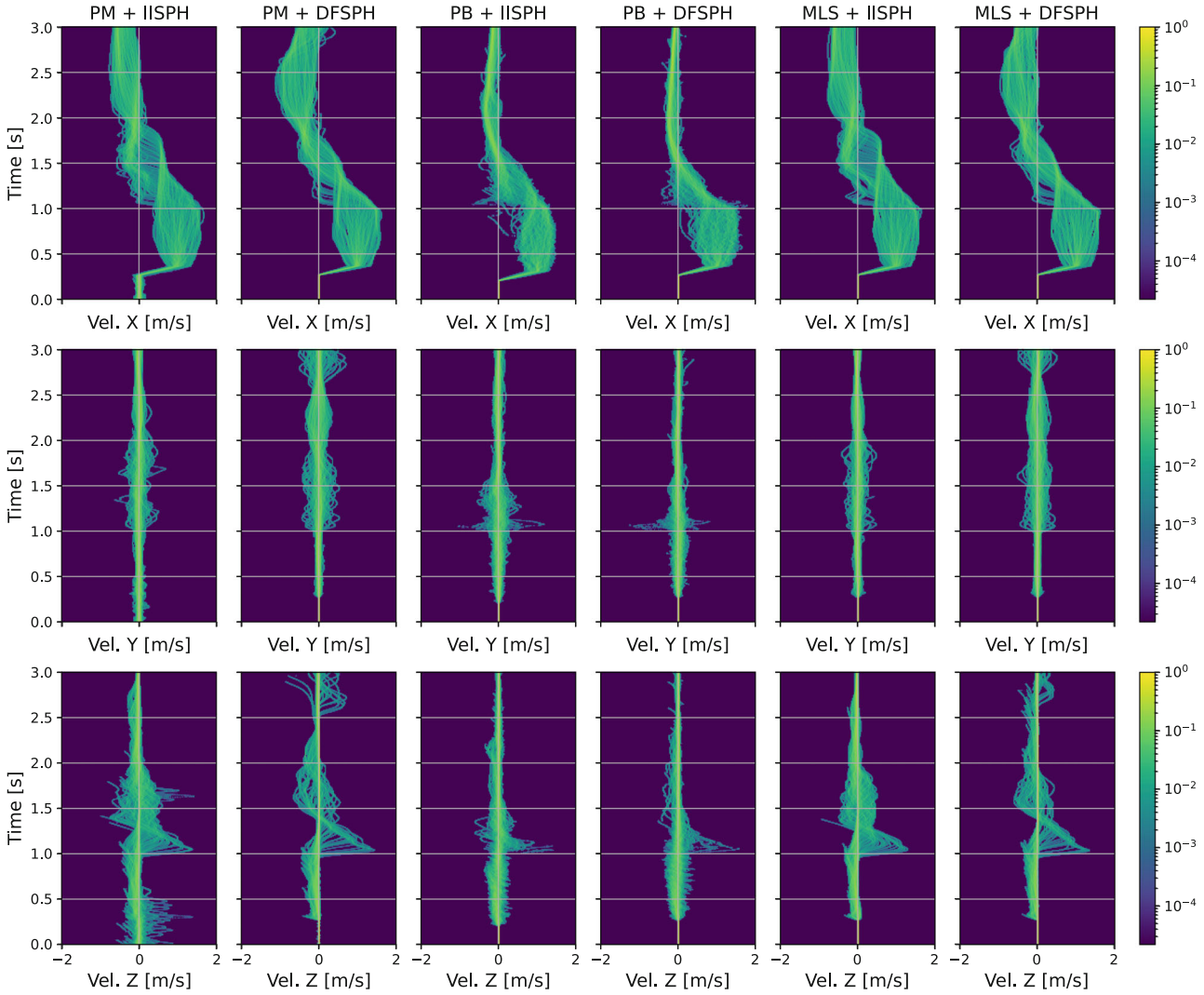

FIGURE 14 Corner motion and impact experiments, fluid sheet. 2D histograms for all three velocity components of all fluid particles. The simulation comprises four stages, relaxation ([0, ∼ .25] s), acceleration ([∼ .25, 1] s), and corner impact including some backflow of particles ([1, 3] s).

TABLE 7 Corner motion and impact experiments, sheet and dambreak experiments.

Experiment	Param	PM+IISPH	PM+DFSPH	PB+IISPH	PB+DFSPH	MLS+IISPH	MLS+DFSPH
Sheet	$\max^{95\%}_{[1,3]s}\ v_z$	9.80e-01	1.14e+00	5.40e-01	3.80e-01	1.02e+00	9.60e-01
	$\sigma_{[1,3]s;\ v_x}$	2.39E-01	2.39E-01	1.28E-01	9.90E-02	2.47E-01	2.21E-01
	$\sigma_{[1,3]s;\ v_y}$	7.32E-02	1.14E-01	6.43E-02	4.92E-02	6.44E-02	9.87E-02
Dambreak	$\max^{95\%}\ v_z$	1.67e+01	1.61e+01	1.63e+01	1.59e+01	1.70e+01	1.65e+01
	$\max^{95\%}\ v_x$	9.86e+00	9.88e+00	9.66e+00	9.63e+00	9.92e+00	9.93e+00
	decay v_x	3.32e+00	3.77e+00	4.14e+00	4.62e+00	3.44e+00	3.78e+00
	σ_{v_y}	2.32e-01	1.33e-01	1.19e-01	1.36e-01	1.38e-01	1.21e-01

Note: The measures $\max^{95\%}$, $\max^{95\%}_{[1,3]s}$, and $\text{stddev}_{[1,3]s}$ refer to the 95% percentile over the full simulation sequence, the 95% percentile over the simulation sequence [1, 3] s, and the average standard deviation over the simulation sequence [1, 3] s, respectively. For the dambreak experiment, the decay is computed as the ratio of the 95% percentile maximum X-velocity peaks of the first and the third reflection at simulation time ∼ 2.5 and ∼ 10 s. Blue colored values are the best values in current row.

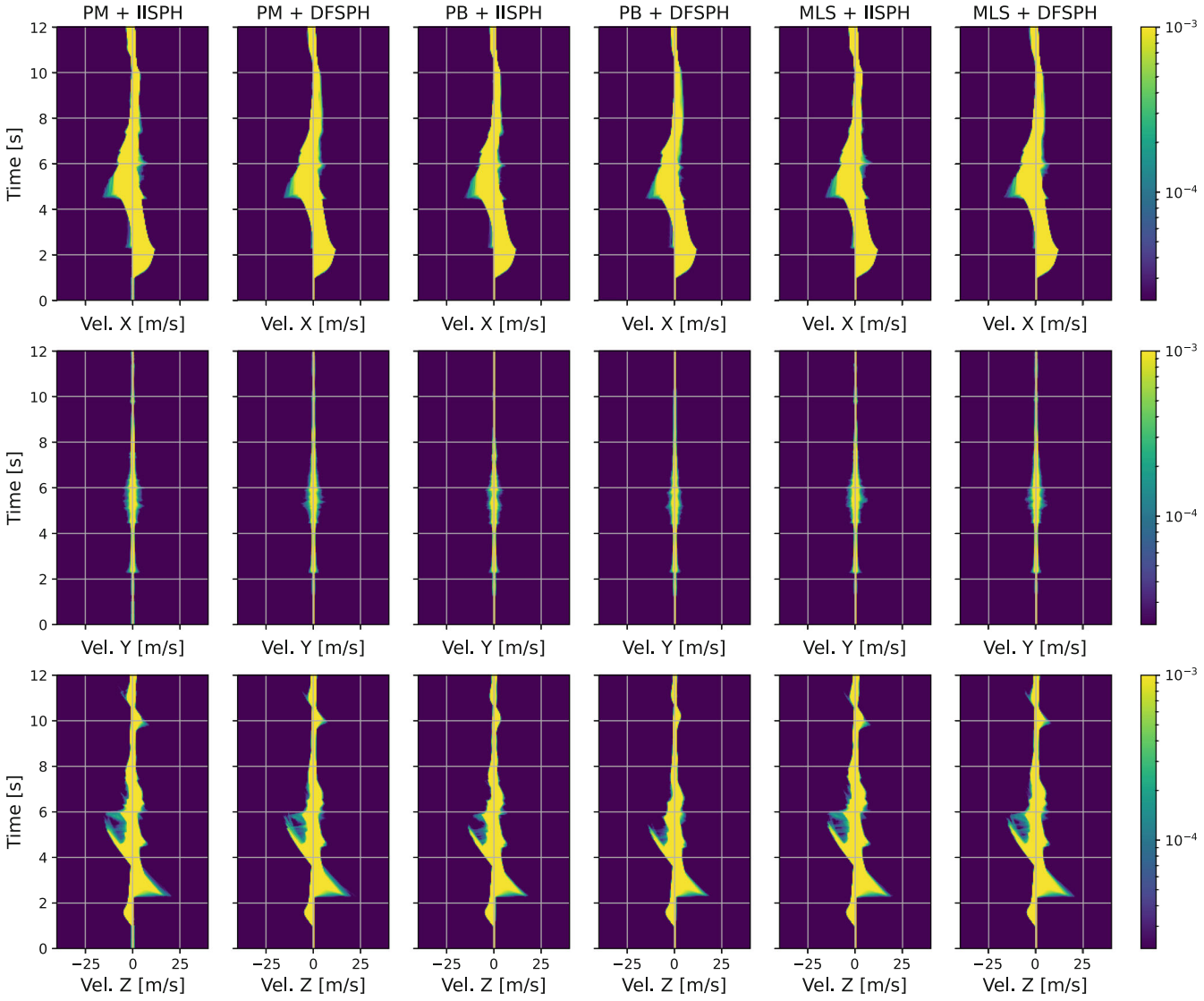

FIGURE 15 Corner motion and impact experiments, dam break experiment. 2D histograms for all three velocity components of all fluid particles.

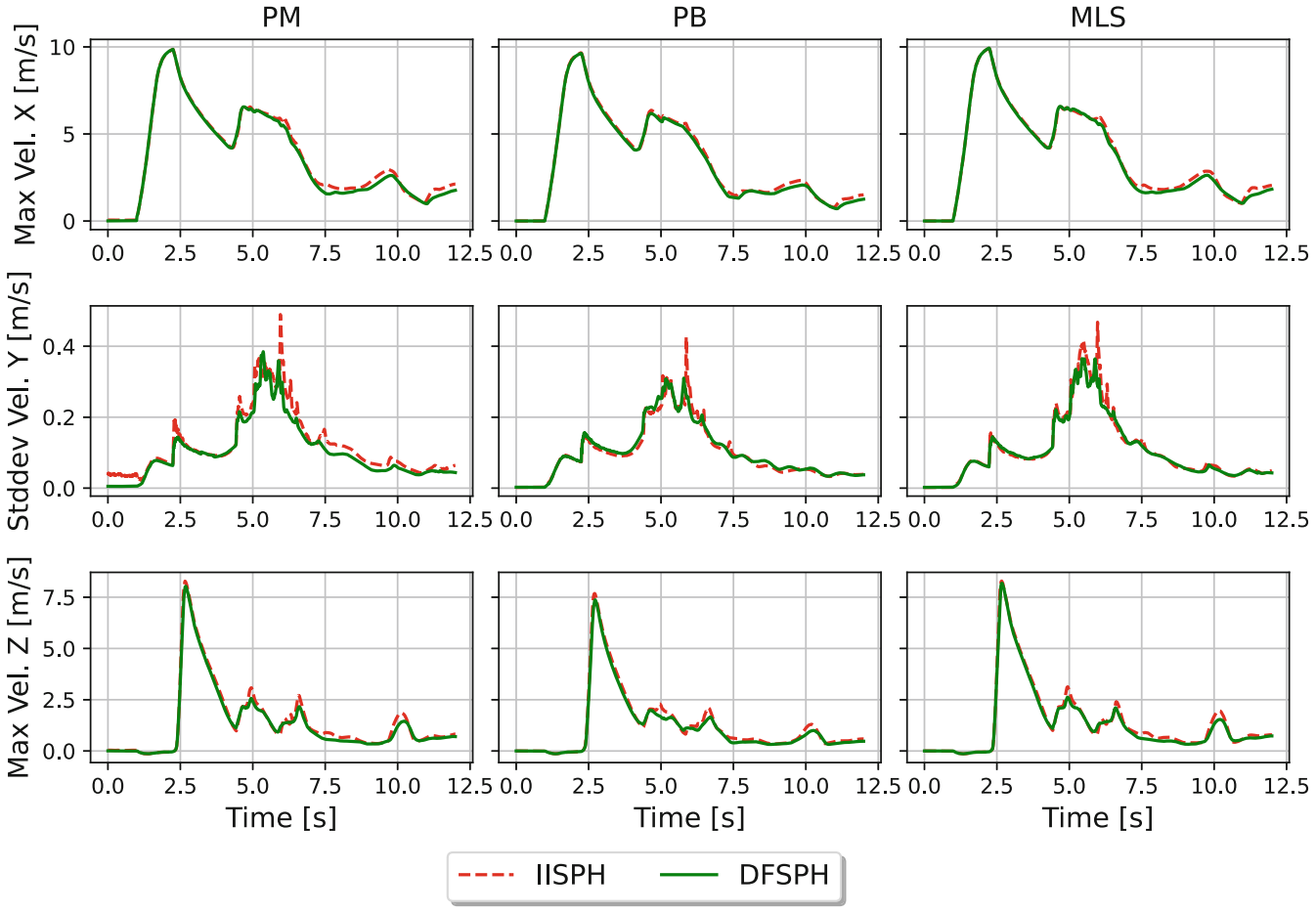

FIGURE 16 Corner motion and impact experiments, dam break experiment. Per-frame statistics for the absolute X, Y, and Z velocity components over time.

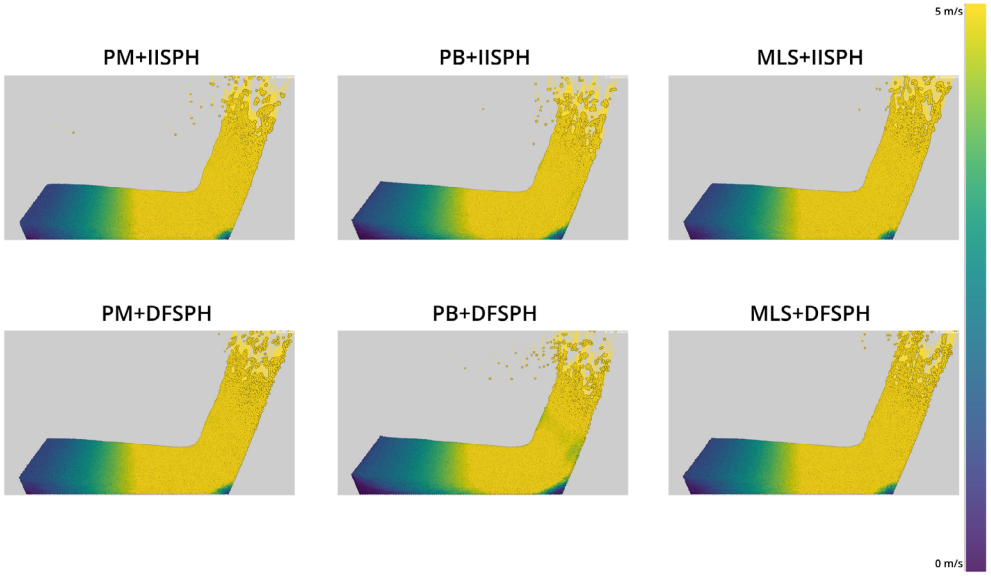

FIGURE 17 Corner motion and impact experiments, dam break experiment. Screenshot of the simulation 5/6 s after dam release.

PM and MLS show the highest velocity magnitudes, which is especially visible in the Z-component at the first impact. Comparing DFSPH and IISPH as fluid solvers, we observe that they behave pretty similar with minor differences. In accordance with the planar boundary experiment, PB shows a high artificial resistance, which is expressed by the decay of v_x. Here, we see higher values of the decay for PB, as well as when the boundary handling method is combined with DFSPH.

From the visual comparison in Figure 17 it is noticeable that PM and MLS have show higher edge of the wave than PB which means that more energy conserved during fluid flow before the impact. In all other visual aspects, all three methods look very alike.

Conclusions

For single particles and fluid sheets, PM and MLS show apparent corner rounding effects for the corner impact experiments, that are, at least for the single particle setting, physically not plausible. PB does not exhibit this effect for a single particle and a fluid sheet to the same extent. Still, looking at more complex experiments, such as the dambreak, the effect is less prominent as it is superimposed by other effects.

5 | RATING SCHEME FOR METHODS

As a result of all performed experiments we accumulate all evaluations for all investigated methods for the different fluid-boundary interaction categories, that is, no motion, tangential motion, normal motion, and corner motion. For each experiment and each measure used in the evaluation, we assign a score. Before assigning the score, we divide the values of the evaluation measures into two ranges: physically reasonable values and physically unreasonable values. For reasonable values we assign positive score and for unreasonable we assign negative score. The range of the score depends on the number of methods compared in the set of experiments. In our case, we investigated six methods and therefore, we score the six methods in the range of $[1, 6]$ (worse to best) for reasonable values and in the range of $[-6, -1]$ (worse to best) for unreasonable values. In our case, the only experiment with unreasonable values is tangential motion experiment for single fluid particle and for fluid sheet (Section 4.3).

Table 8 give the resulting score values for all fluid-boundary interaction categories and fluid configurations. Note, that several experiments contribute to more than one row. The details of the composition of this table and thorough explanations of the ranking procedure are given in the supplementary material.

TABLE 8 Rating table for all methods with weights from 1 to 6.

Motion	Config.	PM+IISPH	PM+DFSPH	PB+IISPH	PB+DFSPH	MLS+IISPH	MLS+DFSPH
No	Single	1.00	1.00	6.00	6.00	1.00	1.00
	Sheet	2.88	2.88	5.00	5.00	4.13	2.63
	Bulk	1.00	2.00	5.00	4.60	4.60	5.60
Tangential	Single	−6.00	−6.00	3.00	3.00	−6.00	−6.00
	Sheet	6.00	6.00	6.00	3.00	2.50	2.50
	Bulk	4.33	4.67	3.67	3.33	3.33	4.00
Normal	Single	6.00	6.00	1.00	1.00	6.00	6.00
	Sheet	4.00	4.00	6.00	6.00	1.00	1.00
	Bulk	5.00	6.00	1.00	1.00	6.00	6.00
Corner	Single	1.00	1.00	6.00	6.00	1.00	1.00
	Sheet	2.00	1.00	5.00	6.00	2.33	1.33
	Bulk	3.50	3.25	4.25	3.25	4.50	3.75

Note: Blue colored values are the best values in current row.

TABLE 9 Shallow water use case.

Motion	Config.	Weight	PM+IISPH	PM+DFSPH	PB+IISPH	PB+DFSPH	MLS+IISPH	MLS+DFSPH
Tangential	Sheet	60%	6.00	6.00	6.00	3.00	2.50	2.50
Corner	Sheet	40%	2.00	1.00	5.00	6.00	2.33	1.33
Total score	-	-	4.40	4.00	5.60	4.20	2.43	2.03

Note: Blue colored values are the best values in current row.

TABLE 10 Pouring water in a glass use case

Motion	Config.	Weight	PM+IISPH	PM+DFSPH	PB+IISPH	PB+DFSPH	MLS+IISPH	MLS+DFSPH
Normal	Bulk	30%	5.00	6.00	1.00	1.00	6.00	6.00
No	Bulk	70%	1.00	2.00	5.00	4.60	4.60	5.60
Total score	-	-	2.20	3.20	3.80	3.52	5.02	5.72

Note: Blue colored values are the best values in current row.

Table 8 is designed to support the decision for a suitable boundary handling method for a given experiment setup. To demonstrate the usage of the ranking table, we consider the following two use cases.

Shallow water: Here, we consider an experiment where we have a shallow water moving back and forth in a closed boundary container. In this case, the fluid in predominantly in a sheet-like configuration, and the fluid motion is mainly tangential and also comprises corner impacts. Consequently, tangential motion is most important in this setting it is weighted with 60% importance, while 40% importance is assigned to corner impact. The "no motion" and "normal motion" situation as well as single particle and bulk configuration are of minor importance (0%). The resulting assessment of all methods yields the highest score for PB+IISPH with 5.60 points (see Table 9). It means in this particular experiment, this methods' configuration would be the best choice.

Pouring water in a glass: In the second use case, a glass is being filled with a bulk of water, where the pouring process and the subsequent relaxation phase of the water is of most interest. We, therefore, weight the normal motion with 30% and the no motion with 70%. In this use case, the highest score is gained by MLS+DFSPH methods' combination with 5.72 points, and MLS is the overall best boundary handling method (see Table 10).

6 | CONCLUSIONS

In this article, we propose an evaluation approach for boundary handling methods in fluid simulation. While our approach is conceptually generic, we mainly address SPH-based fluid simulation and particle-based boundary representation. Our set of 4 experiments presented in 10 experiments is designed to assess all boundary-fluid interaction categories, that is, no motion, tangential motion, normal motion, and corner motion. For each experiment, we describe the simulation setup and the evaluation protocol in detail, and we apply each experiments to three boundary handling methods in SPH, namely PM, PB, and MLS. Our evaluation approach can easily be applied to other boundary handling methods.

We combine all experimental results into a consistent score table and demonstrate how this can be used to identify the most suited boundary handling method for a given simulation setting.

AUTHOR CONTRIBUTIONS

Rustam Akhunov, Rene Winchenbach, and Andreas Kolb equally developed the concept for the experiments and evaluation. Rustam Akhunov set up and carried out the experiments and the evaluation. Rustam Akhunov and Andreas Kolb equally wrote the manuscript with support from Rene Winchenbach. Andreas Kolb supervised the project.

FUNDING INFORMATION

This research was partially funded by the German Research Foundation (DFG) as part of the research project Ko-2960-15/1 "Comprehensive adaptive simulation of SPH-based fluids."

ACKNOWLEDGMENT

Open Access funding enabled and organized by Projekt DEAL.

ORCID

Rustam Akhunov https://orcid.org/0000-0002-4545-6672

REFERENCES

1. Monaghan JJ. Simulating free surface flows with SPH. J Comput Phys. 1994;110(2):399–406.
2. Müller M, Keiser R, Nealen A, Pauly M, Gross M, Alexa M. Point based animation of elastic, plastic and melting objects. Proceedings of the ACM SIGGRAPH/Eurographics Symposium on Computer Animation; 2004. p. 141–51.
3. Akinci N, Ihmsen M, Akinci G, Solenthaler B, Teschner M. ACM Trans Graph. 2012;31(4):1–8.
4. Harada T, Koshizuka S, Kawaguchi Y. Smoothed particle hydrodynamics in complex shapes. Proceedings of the Spring Conference on Computer Graphics; 2007. p. 191-7.
5. Fujisawa M, Miura KT. an efficient boundary handling with a modified density calculation for SPH. Comput Graph Forum. 2015;34(7):155–62.
6. Band S, Gissler C, Peer A, Teschner M. MLS pressure boundaries for divergence-free and viscous SPH fluids. Comput Graph. 2018;76:37–46.
7. Band S, Gissler C, Ihmsen M, Cornelis J, Peer A, Teschner M. Pressure boundaries for implicit incompressible SPH. ACM Trans Graph. 2018;37(2):1–11.
8. Nomeritae DE, Grimaldi S, Bui HH. Explicit incompressible SPH algorithm for free-surface flow modelling: a comparison with weakly compressible schemes. Adv Water Resour. 2016;97:156–67.
9. Farzin S, Fatehi R, Hassanzadeh Y. Position explicit and iterative implicit consistent incompressible SPH methods for free surface flow. Comput Fluids. 2019;179:52–66.
10. Ferrand M, Laurence DR, Rogers BD, Violeau D, Kassiotis C. Unified semi-analytical wall boundary conditions for inviscid, laminar or turbulent flows in the meshless SPH method. Int J Numer Methods Fluids. 2013;71(4):446–72.
11. Shadloo MS, Zainali A, Yildiz M, Suleman A. A robust weakly compressible SPH method and its comparison with an incompressible SPH. IntJ Numer Methods Eng. 2012;89:939–56.
12. Mayrhofer A, Rogers BD, Violeau D, Ferrand M. Investigation of wall bounded flows using SPH and the unified semi-analytical wall boundary conditions. Comput Phys Commun. 2013;11:2515–27.
13. Band S, Gissler C, Teschner M. Moving least squares boundaries for SPH fluids. VRIPHYS; 2017.
14. SPHERIC validation tests. https://spheric-sph.org/validation-tests
15. Heller V, Hager WH, Minor HE. Landslide generated impulse waves in reservoirs: basics and computation. VAW-Mitteilungen. 2009;211.
16. Delorme L, Colagrossi A, Souto-Iglesias A, Zamora-Rodriguez R, Botia-Vera E. A set of canonical problems in sloshing, Part I: pressure field in forced roll-comparison between experimental results and SPH. Ocean Eng. 2009;36(2):168–78.
17. Issa R, Violeau D. Test-case 2, 3D dambreaking, release 1.1 ERCOFTAC. SPH European research interest community SIG, Electricite De France, Laboratoire National Hydaulique et Environnement; 2006.
18. Koschier D, Bender J, Solenthaler B, Teschner M. Smoothed particle hydrodynamics techniques for the physics based simulation of fluids and solids. Eurographics 2019 -tutorials; 2019. p. 1–41.
19. Koschier D, Bender J, Solenthaler B, Teschner M. A survey on SPH methods in computer graphics. Computer graphics forum. Volume 41. New York: Wiley Online Library; 2022. p. 737–60.
20. Ihmsen M, Cornelis J, Solenthaler B, Horvath C, Teschner M. Implicit incompressible SPH. IEEE Trans Visual Comput Graph. 2014;20(3):426–35.
21. Bender J, Koschier D. Divergence-free SPH for incompressible and viscous fluids. IEEE Trans Visual Comput Graph. 2017;23(3):1193–206.
22. Gingold RA, Monaghan JJ. Smoothed particle hydrodynamics: theory and application to non-spherical stars. Monthly Not Royal Astron Soc. 1977;12:375–89.
23. Koschier D, Bender J. Density maps for improved SPH boundary handling; 2017.
24. Gissler C, Peer A, Band S, Bender J, Teschner M. Interlinked SPH pressure solvers for strong fluid-rigid coupling. ACM Trans Graph. 2019;38(1):1–13.
25. Winchenbach R, Akhunov R, Kolb A. ACM Trans Graph. 2020;39:1–17.
26. Crespo AC, Dominguez JM, Barreiro A, Gómez-Gesteira M, Rogers BD. GPUs, a new tool of acceleration in CFD: efficiency and reliability on smoothed particle hydrodynamics methods. PLoS One. 2011;6(6):e20685.
27. Monaghan JJ, Kos A. Solitary waves on a Cretan beach. J Waterway Port Coast Ocean Eng. 1999;125(3):145–55.

28. Lee E, Violeau D, Issa R, Ploix S. Application of weakly compressible and truly incompressible SPH to 3-D water collapse in waterworks Application de SPH faiblement compressible et vraiment incompressible à l'écrasement 3D de l'eau sur des ouvrages hydrauliques; 2010.
29. Morris JP, Fox PJ, Zhu Y. Modeling low Reynolds number incompressible flows using SPH. J Comput Phys. 1997;136(1):214–26.
30. Bender J, Kugelstadt T, Weiler M, Koschier D. Volume maps: an implicit boundary representation for SPH. Motion, interaction and games. New York: ACM Digital Library; 2019. https://doi.org/10.1145/3359566.3360077
31. Liu S, Nistor I, Mohammadian M. Evaluation of the solid boundary treatment methods in SPH. Int J Ocean Coastal Eng. 2018;1(2):1840002.
32. Crespo AJ, Gómez-Gesteira M, Dalrymple RA. Boundary conditions generated by dynamic particles in SPH methods. Comput Mater Continu. 2007;5(3):173–84.
33. English A, Domínguez JM, Vacondio R, Crespo AJ, Stansby PK, Lind SJ, et al. Modified dynamic boundary conditions (mDBC) for general-purpose smoothed particle hydrodynamics (SPH): application to tank sloshing, dam break and fish pass problems. Comput Part Mech. 2021;04:1–15.
34. Hui PJ, Shao S, Huang Y, Hussain K. Evaluations of SWEs and SPH numerical modelling techniques for dam break flows. Eng Appl Comput Fluid Mech. 2013;7(4):544–63.
35. Monaghan JJ, Kajtar JB. SPH particle boundary forces for arbitrary boundaries. Comput Phys Commun. 2009;180(10):1811–20.
36. Mayrhofer A, Ferrand M, Kassiotis C, Violeau D, Morel FX. Unified semi-analytical wall boundary conditions in SPH: analytical extension to 3-D. Numer Algor. 2015;68(1):15–34.
37. Long T, Hu D, Wan D, Zhuang C, Yang G. An arbitrary boundary with ghost particles incorporated in coupled FEM-SPH model for FSI problems. J Comput Phys. 2017;350:166–83.
38. Huber M, Reinhardt S, Weiskopf D, Eberhardt B. Evaluation of surface tension models for SPH-based fluid animations using a benchmark test. VRIPHYS; 2015:41-50.
39. Rakhsha M, Yang L, Negrut D. A comparison of three SPH methods for the solution of the Fluid-Solid Interaction problem. APS Division of Fluid Dynamics Meeting Abstracts; 2019. p. H07–009.
40. Sheikh B, Qiu T, Ahmadipur A. Comparison of SPH boundary approaches in simulating frictional soil–structure interaction. Acta Geotechn. 2021;16(8):2389–408.
41. Becker M, Tessendorf H, Teschner M. Direct forcing for Lagrangian rigid-fluid coupling. IEEE Trans Vis Comput Graph. 2009;15(3):493–503.
42. Bell N, Yu Y, Mucha P. Particle-based simulation of granular material. Proceedings of the ACM SIGGRAPH/Eurographics Symposium Computer Animation; 2005. p. 77–86.
43. Winchenbach R. Framework zur effektiven Umsetzung von Fluidsimulationen auf GPU. Master thesis. Computer Graphics Group, University of Siegen; 2018.
44. Monaghan JJ. Smoothed particle hydrodynamics. Rep Progr Phys. 2005;68(8):1703–59. https://doi.org/10.1088/0034-4885/68/8/r01
45. Akinci N, Akinci G, Teschner M. Versatile surface tension and adhesion for SPH fluids. ACM Trans Graph (TOG). 2013;32(6):1–8.
46. Boxer G. Hydrostatic pressure. Fluid mechanics. New York: Springer; 1988. p. 8–30.
47. Vaserstein LN. Markov processes over denumerable products of spaces, describing large systems of automata. Probl Peredachi Informat. 1969;5(3):64–72.
48. Schlicker S, Austin D, Boelkins M. Active calculus multivariable: 2018 edition; 2018.

AUTHOR BIOGRAPHIES

Rustam Akhunov received the M.Sc. degree from the Technical University of Gdansk, Poland, in 2018. Now he is currently a Ph.D. Student under Andreas Kolb at the University of Siegen, Germany. His research interests include particle-based fluid simulation, numerical methods.

Rene Winchenbach received his Ph.D. from the University of Siegen, Germany, in 2021, and he currently works at the Technical University Munich, Germany, as a postdoctoral researcher under Nils Thuerey. His research interests include particle-based fluid simulation, numerical methods, spatial adaptivity and the interplay of deep learning and physics-based simulations.

Andreas Kolb received the Ph.D. degree from the University of Erlangen, Germany, in 1995. He is currently the Head of the Computer Graphics and Multimedia Systems Group, University of Siegen, Germany. His research interests include computer graphics and computer vision, including particle-based simulation and visualization, as well as GPU-based simulation, processing, and visualization of sensor data.

SUPPORTING INFORMATION

Additional supporting information can be found online in the Supporting Information section at the end of this article.

How to cite this article: Akhunov R, Winchenbach R, Kolb A. Evaluation of particle-based smoothed particle hydrodynamics boundary handling approaches in computer animation. Comput Anim Virtual Worlds. 2023;34(6):e2138. https://doi.org/10.1002/cav.2138